This document is confidential and is proprietary to the American Chemical Society and its authors. Do not copy or disclose without written permission. If you have received this item in error, notify the sender and delete all copies.

Structural Evolution and Photoluminescence Quenching Across the $FASnI_{3-x}Br_x$ (x = 0 - 3) Perovskites

Journal:	Journal of the American Chemical Society
Manuscript ID	ja-2024-03669p.R1
Manuscript Type:	Article
Date Submitted by the Author:	29-Apr-2024
Complete List of Authors:	Balvanz, Adam; Northwestern University, Chemistry Safdari, Majid; Northwestern University, Department of Chemistry Zacharias, Marios; INSA Rennes, FOTON Insitute Kim, Daehan; Northwestern University, Department of Chemistry Welton, Claire; Unité de Catalyse et Chimie du Solide Oriel, Evan; Northwestern University, Chemistry Kepenekian, Mikaël; Institut des Sciences Chimiques de Rennes, Katan, Claudine; Univ Rennes, ISCR (Institut des Sciences Chimiques de Rennes) Malliakas, Christos; Northwestern University, Chemistry Even, Jacky; FOTON, INSA Rennes Klepov, Vladislav; University of Georgia, Chemistry Manjunatha Reddy, G N; Universite de Lille, Chemistry Schaller, Richard; Northwestern University, Department of Chemistry Chen, Lin; Argonne National Laboratory, Chemical Sciences and Engineering; Northwestern University, Department of Chemistry Seshadri, Ram; University of California Santa Barbara, Materials; UC Santa Barbara, Materials Kanatzidis, Mercouri; Northwestern University, Department of Chemistry

SCHOLARONE™ Manuscripts

Structural Evolution and Photoluminescence Quenching Across the FASnI_{3-x}Br_x (x = 0 - 3) Perovskites

Adam Balvanz,¹ Majid Safdari,^{1,2*} Marios Zacharias,³ Daehan Kim,¹ Claire Welton,⁴ Evan H. Oriel,¹ Mikaël Kepenekian,⁵ Claudine Katan,⁵ Christos D. Malliakas,¹ Jacky Even,³ Vladislav Klepov,^{1,6} G.N. Manjunatha Reddy,⁴ Richard D. Schaller,^{1,7} Lin X. Chen,^{1,8} Ram Seshadri,⁹ and Mercouri G. Kanatzidis^{1*}

¹Northwestern University Department of Chemistry, Evanston, IL 60208 USA

²Department of Chemistry, Division of Applied Physical Chemistry, KTH Royal Institute of Technology, SE-100 44 Stockholm, Sweden

³ Univ Rennes, INSA Rennes, CNRS, Institute FOTON – UMR 6082, Rennes F-35000, France

⁴University of Lille, CNRS, Centrale Lille, Univ. Artois, UMR 8181 – UCCS – Unité de Catalyse et Chimie du Solide, Lille F-59000, France

⁵Univ Rennes, INSA Rennes, CNRS, ISCR – UMR 6226, Rennes F-35000, France

⁶University of Georgia Department of Chemistry, Athens, GA 30602 USA

⁷Center for Nanoscale Materials, Argonne National Laboratory, Lemont, IL 60439 USA

⁸Materials Science Division, Argonne National Laboratory, Lemont, IL 60439 USA

⁹Materials Department and Materials Research Laboratory, University of California, Santa Barbara, CA 93106, USA

^{*}Correspondence: m-kanatzidis@northwestern.edu; majid.safdari@northwestern.edu

Abstract:

One of the primary methods for band gap tuning in metal halide perovskites has been halide (I/Br) mixing. Despite widespread usage of this type of chemical substitution in perovskite photovoltaics, there is still little understanding of the structural impacts of halide alloying, with the assumption being the formation of ideal solid solutions. The FASnI_{3-x}Br_x (x = 0 - 3) family of compounds provides the first example where the assumption breaks down, as the composition space is broken into two unique regimes (x = 0 - 2.9; x = 2.9 - 3) based on their average structure with the former having a 3D and the latter having an extended 3D (pseudo 0D) structure., Pair distribution function (PDF) analyses further suggest a dynamic $5s^2$ lone pair expression resulting in increasing levels of off-centering of the central Sn as the Br concentration is increased. These antiferroelectric distortions indicate that even the x = 0 - 2.9 phase space behaves as a non-ideal solid-solution on a more local scale. Solid State NMR confirms the difference in local structure yielding greater insight into the chemical nature and local distributions of the FA⁺ cation. In contrast to the FAPbI_{3-x}Br_x series, a drastic photoluminescence (PL) quenching is observed with x > 1.9 compounds having no observable PL. Our detailed studies attribute this quenching to structural transitions induced by the distortions of the [SnBr₆] octahedra in response to stereochemically expressed lone pairs of electrons. This is confirmed through density functional theory, having a direct impact on the electronic structure.

1.0 Introduction:

Three-dimensional metal halide perovskites (MHPs) have been a major focus of ongoing research in the realm of photovoltaics (PV) due to their superior optoelectronic properties. These compounds are direct-gap, strong light-absorbing semiconductors with high carrier mobilities and high tolerance to defect states. 1-7 These favorable properties have allowed for a rapid improvement of perovskite-based PV, exceeding traditional Si-based devices in more recent years. Single junction perovskite solar cells (PSCs) first showed viability, achieving a power conversion efficiency (PCE) of ~11\%^{8,9} and has since rapidly improved, ¹⁰ achieving closer to the theoretical Shockley-Queisser limit (33.7%) with recent examples of single junction devices having >25% PCE. 11-14 Tuning the bandgap for Pb perovskites was successfully performed through the variation of the chemical composition, i.e., by I/Br and/or Pb/Sn mixing. 15-17 These new compositions across the mixed iodide-bromide phase space possess a well-behaved three-dimensional network leading to improved phase stability¹⁸ and monumental efficiency improvements for related solar cells. This includes the mixed cation/halide perovskite used in 31.2% of perovskite/silicon tandem devices.¹⁹ Although there has been success with these phases, there are serious issues with the perovskite layer in a functional solar cell as the perovskite undergoes phase segregation under illumination due to halide migration.²⁰⁻²²

While the highest performing devices use lead (Pb) based halide perovskites and tandem cells use the mixed halide (I/Br) variant, ²³⁻²⁵ considerable effort has been made to create Pb-free PSCs due to Pb's toxicity. ²⁶ One way of addressing these concerns is by using the ASnX₃ compositions. Sn²⁺ based materials have also shown success as light-absorbing layers, but the PCE lags behind only reaching ~14% for a single junction device: a considerable compromise in performance. ²⁷ This can be attributed to a number of factors, including the instability of the Sn²⁺ oxidation state, making it more difficult to suppress the creation of performance-killing Sn⁴⁺ defect states. Nonetheless, due to their structural versatility for compositional management and the existing knowledge of their Pb counterparts, Sn-based PSC are expected to improve in terms of stability and device performance as active research continues. ²⁸⁻³⁰

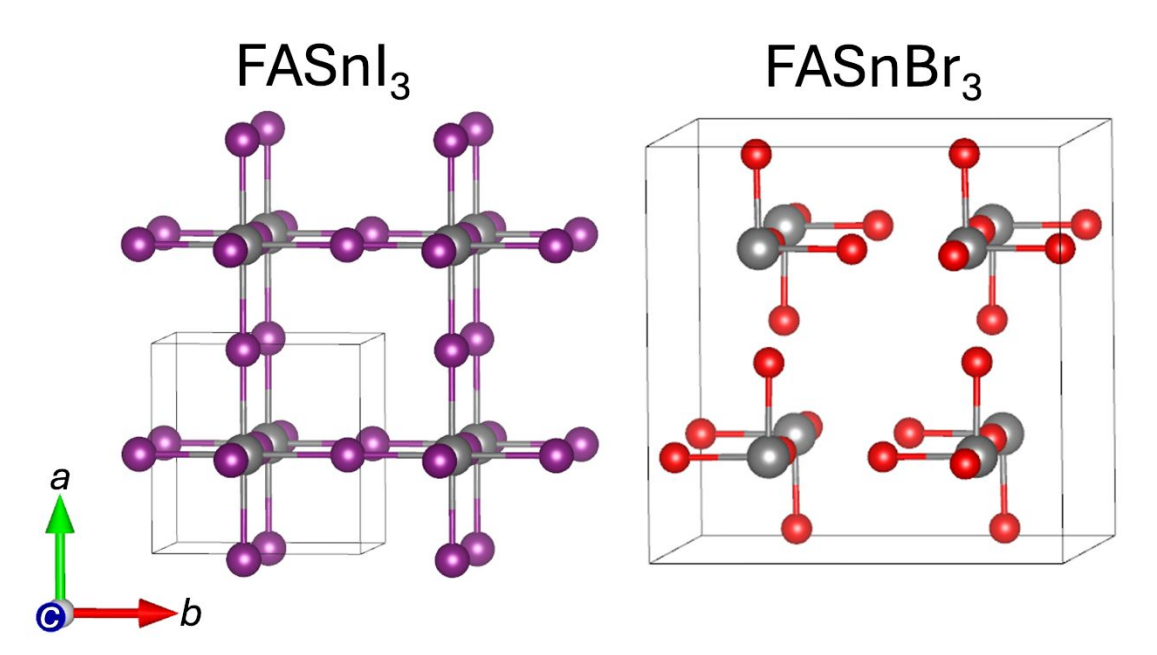


Figure 1: Depicts the 3D inorganic framework of FASnI₃ (left) and the extended 3D framework of FASnBr₃ (right). The atoms are presented as grey, purple, and red for Sn, I, and Br respectively. the FA⁺ cations are omitted for simplicity. FASnI₃ and FASnBr₃ are modeled in $Pm\overline{3}m$ and $Pa\overline{3}$ respectively.

In this vein, we need a holistic understanding of the structural complexities of hybrid mixed halide perovskites. We chose the representative family of compounds called FASnI_{3-x}Br_x (where x = 0 - 3) because they have a remarkably broad range of band gap energies and exhibit structural complexity due to the diverse room temperature structures of FASnI₃ and FASnBr₃. ^{31, 32} FASnI₃ crystallizes with a typical 3D perovskite framework with SnI₆ octahedra corner sharing in all directions and the FA⁺ cation filling the central voids, counterbalancing the overall negative charge. FASnBr₃, on the other hand, has a structure that is atypical of MHPs based on increased expression of the Sn $5s^2$ lone pair, leading to significant off-centering. The compound deviates from the ideal 3D perovskite framework by lengthening three Sn – Br bonds and shortening the other three in the SnBr₆ octahedra in a coherent fashion, forming what can be thought of as more discrete pyramidal 0D [SnBr₃]⁻ units. Since the orientation and arrangement of these molecular units in space retains the original undistorted architecture, the structure can still be thought of as a 3D perovskite type. The FA⁺ cations then occupy positions within this "distorted cage" to balance the charge (Figure 1).

Here, we study the FASnI_{3-x}Br_x (x = 0 - 3) chemical substitution range. Analysis of the average crystal structures shows a composition-dependence splitting the space into two unique regimes, apparently indicating non-idealistic behavior expected for a solid-solution. The x = 0 –

2.9 range adopts an average structure in line with the FASnI₃ structure type, and the x = 2.9 - 3range takes on the FASnBr₃ room temperature structure with lower symmetry. However, inspection of the thermal displacement and lattice parameters suggests that the structure modification is already present at the local scale for x < 2.9. Single crystal X-ray diffraction analysis, thus, provides evidence for a more gradual structural evolution from the FASnI₃ to the FASnBr₃ structure type, initially exhibiting antiferroelectric distortions at the local scale that finally exhibits long-range ordering. We also find that careful control of the synthetic conditions is necessary to produce bulk crystallites with the desired I/Br ratio in the final product, as the typical synthetic procedures in hydrohalic acid solutions show a non-linear behavior. Furthermore, halide substitution drastically impacts the photoluminescence (PL) as there is a significant decrease in PL intensity with the introduction of Br. PL intensity decreases between x = 0 - 1.1, finally falling below the background with no observable emission present for $x \ge 1.9$. Further investigation revealed the above-mentioned systematic structural distortions as the most dominant source for PL quenching in high bromide compositions. The distortions provide a rationale for quenching of the photoluminescence with Br incorporation as the structure distorts and the $5s^2$ lone pair becomes more stereochemically expressed. This suggested mechanism is bolstered by room temperature Raman spectroscopy and pair distribution function (PDF) measurements which show unique scattering signatures and distance vectors for predominantly Br-rich molecular $[SnBr_{3-x}I_x]^2$ type units, and DFT calculations focusing on the activity of the Sn $5s^2$ lone pair of electrons. Solid state NMR also supports the difference in framework closely associated with the Br concentration. Specifically, the FA⁺ cation shows sharper signatures in the ¹H spectrum of Brrich samples, meaning its motion has more fluidity. These findings are in contrast to PL behavior for the APbI_{3-x}Br_x (x = 0 - 3; A = MA, FA) analogues, which show consistent PL response across the substitution range.^{33, 34} This study serves as a reminder that structural considerations in compositionally complex MHPs are paramount in understanding the behavior of the materials' performance for optoelectronic applications.

2.0 Materials and Methods:

2.1. General Synthetic Approach: Each of the compounds presented in this study was synthesized using solution-based crystal growth techniques in hydrohalic acid, which is a methodology that has been used on countless occasions by our research team to grow hybrid 3D and 2D phases

alike.^{7, 31, 35-37} The variant of the precipitation reaction used to synthesize materials in the FASnI₃. $_x$ Br $_x$ (x = 0 - 3) family was as follows: desired quantities of SnCl₂·2H₂O (Sima-Aldrich; 98 wt.%) were dissolved in a solution comprised of hydroiodic (Sigma-Aldrich 57 wt.% in H₂O), hydrobromic (Sigma-Aldrich; 48 wt.% in H₂O), and hypophosphorous acids (Sigma-Aldrich; 50 wt.% in H₂O) under constant stirring while on a hotplate set to ~120°C (Table 1). The hypophosphorous acid was added as a necessary reducing reagent utilized to suppress the oxidation of Sn²⁺ to Sn⁴⁺ as well as to prevent the conversion of I⁻ to [I₃]^{3-,35} Once the solid was dissolved, desired amounts of formamidine acetate (FACH₃COO; TCI; >98 wt.%) were added to the hot reaction, followed immediately by the rapid crystallization of the desired perovskite phase, the persistence of which was dependent on the ratio of the hydrohalic acids (I-rich generally persisted longer than Br-rich). The temperature of the hotplate was then increased to ~210 °C while stirring continued until the solid dissolved and a clear solution was achieved. The reaction was then allowed to cool to room temperature, where the perovskite phase precipitated from the solution and could be extracted for further measurements.

Table 1: Experimental conditions used for the synthesis of the FASnI_{3-x}Br_x compounds. The volume percentages are based on the ratio of the two hydrohalic acids added to the reaction solution not considering contributions from the hypophosphorous acid.

Compound	HI (vol.%)	HBr (vol.%)	Mol Fraction χ _{HBr}
FASnI ₃	100	0	0
$FASnI_{2.6}Br_{0.4}$	66	34	0.38
$FASnI_{2.3}Br_{0.7}$	34	66	0.69
$FASnI_{2.1}Br_{0.9}$	25	75	0.78
$FASnI_{1.9}Br_{1.1}$	33	67	0.70
$FASnI_{1.1}Br_{1.9}$	17	83	0.85
$FASnI_{0.7}Br_{2.3}$	8	92	0.93
$FASnI_{0.4}Br_{2.6}$	7	93	0.94
$FASnI_{0.1}Br_{2.9}$	3	97	0.97
FASnBr ₃	0	100	1

In our experience, the perovskite phase needed to be extracted once the reaction reached room temperature. As the solid continued to remain in solution, halide exchange was observed with a darkening of the crystals over time. The color of the perovskite phase varied from black (iodide rich) to yellow (bromide rich) depending on the overall ratio of I/Br incorporation (Figure 2b). For more specific synthetic details, the reader is referred to the supporting information for the synthesis conditions for each of the products. Since the samples were all susceptible to oxidation when removed from the mother liquor, the crystals were dried inside a nitrogen-filled glove box or under a vacuum. Air-free powder diffraction patterns were collected to confirm the identity of

the bulk material (Figure S1), and semiquantitative scanning electron microscopy coupled with energy dispersive X-ray spectroscopy (SEM-EDS) then confirmed the elemental composition (Table S5).

2.2 Powder X-ray Diffraction (PXRD): Dry crystallites were ground inside a N₂-filled glovebox with a mortar and pestle until a powder-like consistency was achieved. The powder was then packed into an 8 mm metallic mask with the usage of two polyimide layers of tape (one on both sides of the mask). The PXRD data were then collected at room temperature on a STOE-STADI-P powder diffractometer equipped with an asymmetric curved Germanium monochromator which uses Cu $K_{\alpha 1}$ ($\lambda = 1.54056$ Å) radiation for diffraction and a MYTHEN2 1K DECTRIS one-dimensional silicon strip detector. The intensity data were collected within the range 5-60° 2θ . The instrument was first calibrated against a NIST Silicon standard (640d) prior to diffraction.

2.2.0 Single Crystal X-ray Diffraction Data for $FASnI_{3-x}Br_x$ (x = 0 - 3) Phases at Room Temperature

Table 2: Selected Crystallographic information and refinement statistics for representative FASnI_{3-x}Br_x (x = 0 - 3) compositions. FASnI₃ and FASnBr₃ were synthesized and measured independently of previous research efforts. The full Table can be found in the supporting information Table S1.

Formula	FASnI ₃	FASnI _{2.6} Br _{0.4}	FASnI _{2.3} Br _{0.7}	FASnI _{2.1} Br _{0.9}	FASnI _{1.9} Br _{1.1}	FASnI _{1.1} Br _{1.9}	FASnI _{0.7} Br _{2.3}	FASnI _{0.4} Br _{2.6}	FASnI _{0.1} Br _{2.9}	FASnBr ₃
Formula weight	525.41	518.74	508.41	495.72	488.67	452.02	432.28	418.19	402.62	398.45
Space group	$Pm^{\overline{3}}m$	$Pm^{\overline{3}}m$	$Pm^{\overline{3}}m$	$Pm^{\overline{3}}m$	$Pm^{\overline{3}}m$	$Pm^{\overline{3}}m$	$Pm^{\overline{3}}m$	$Pm^{\overline{3}}m$	$Pa^{\overline{3}}$	$Pa^{\overline{3}}$
a/b/c (Å)	6.3064(3)	6.3099(2)	6.2824(2)	6.2525(5)	6.2449(1)	6.1354(2)	6.0915(2)	6.0443(2)	12.0637(15)	12.0303(5
Volume (ų)	250.81(4)	251.23(3)	247.96(2)	244.43(6)	243.54(1)	230.96(6)	226.03(2)	220.82(2)	1755.7(7)	1741.1(2)
ž ´	1	1	1	1	1	1	1	1	8	8
ρ _{calc} (g/cm ³) Absorption	3.479	3.429 12.080	3.405 12.441	3.368 12.871	3.332 13.058	3.250 14.537	3.176 15.275	3.145 15.944	3.046 8.707	3.040 16.615
coefficient (mm ⁻¹)	11.695									
Independe nt	91 [R _{int}	$172 [R_{int} = 0.0117]$	$166 [R_{int} = 0.0087]$	$103 [R_{int} = 0.0314]$	$160 [R_{int} = 0.0183]$	$68 [R_{int} = 0.0750]$	$95 [R_{int} = 0.0136]$	$113 [R_{int} = 0.0132]$	$688 [R_{int} = 0.0487]$	$641 [R_{int}]$ = 0.0716]
reflections	0.0375]	***************************************	,						,	
Data / restraints / parameters	91 / 1 / 8	172 / 1 / 10	166 / 1 / 10	103 / 1 / 9	160 / 1 / 10	68 / 1 / 9	95 / 1 / 10	113 / 1 / 10	688 / 2 / 25	641 / 2 / 24
Final R indices [I > 2σ(I)]	$R_{obs} = 0.0435,$ $wR_{obs} = 0.01248$	$\begin{array}{l} R_{obs} = 0.0231, \\ wR_{obs} = \\ 0.0766 \end{array}$	$R_{obs} = 0.0239,$ $wR_{obs} =$ 0.0877	$R_{obs} = 0.0429,$ $wR_{obs} =$ 0.1006	$R_{obs} = 0.0231,$ $wR_{obs} =$ 0.0846	$R_{obs} = 0.0292,$ $wR_{obs} =$ 0.0950	$R_{obs} = 0.0317,$ $wR_{obs} =$ 0.1092	$R_{obs} = 0.0479,$ $wR_{obs} =$ 0.1540	$R_{obs} = 0.0585,$ $wR_{obs} =$ 0.1451	$R_{obs} = 0.0419,$ $wR_{obs} = 0.1011$
Largest diff. peak/hole (e·Å-3)	0.869/- 1.372	0.680/-0.836	1.229/-1.299	0.656/-0.944	0.814/-0.828	0.716/-0.4	0.636/-0.610	0.747/-1.260	0.952/-0.695	0.799/- 0.643

Single crystals within the FASnI_{3-x}Br_x (x = 0 - 3) range were extracted from the mother liquor and immediately placed under Paratone-N oil on a glass slide to protect the surface from oxidation. The crystals were then transported to an optical microscope where suitable crystals were

selected, cut to size, and mounted onto the goniometer head of a single crystal diffractometer for collection. An inert environment was maintained throughout the collections through the usage of a nitrogen blanket, which was sourced from the liquid, through an Oxford Cryosystems cryostat. This proved to be necessary in order to preserve the desired perovskite phase during diffraction as each of the samples was susceptible to oxidation with exposure to ambient conditions. Intensity data was then collected on either a STOE Stadi Vari diffractometer, which uses an AXO Ag Ka micro-focus sealed X-ray A-MiXS source for diffraction ($\lambda = 0.560834$ Å) and a Dectris Platus 3 R CdTe 300 K Hybrid Photon Counting Detector, or a XtaLAB Synergy diffractometer, equipped with a microfocus sealed X-ray tube PhotonJet (Mo K_a : $\lambda = 0.71073$ Å) for diffraction and a Hybrid Pixel Array Detector (HyPix). The data collected on the Stadi Vari diffractometer was then reduced using the X-area software package (STOE). LANA³⁸ was used to perform a semi-empirical absorption correction through outlier rejection and scaling of the reflections. The reduction for the data collected on the Synergy diffractometer was done within the CrysAlisPro software package (Rigaku) using an empirical absorption correction. For all of the room temperature data sets, the reflections were then imported into Olex2³⁹ where the data was solved using the intrinsic phrasing method as implemented in ShelXT⁴⁰ and further refined using least squares on F^2 with ShelXL.⁴¹ Selected crystallographic information and refinement statistics are presented in Table 2.

2.2.1: Low Temperature Single Crystal X-ray Diffraction: Low temperature diffraction experiments were conducted on freshly synthesized FASnI_{1.9}Br_{1.1} and FASnI_{0.4}Br_{2.6} crystals using the STOE Stadi Vari diffractometer discussed in the previous section. Measurements were conducted at various temperatures which were maintained through a flow of N₂ gas, obtained from the liquid, sustained by an Oxford Cryostream 700 plus cryostat. Data reduction was accomplished in the X-area software (STOE), using a semi-empirical absorption correction, outlier rejection, and frame scaling as applied in LANA.³⁸ FASnI_{0.4}Br_{2.6} showed a phase transition at 260 K and the low temperature structure was elucidated in Jana2006⁴² due to increased disorder where a structural solution was achieved through SUPERFLIP⁴³ and refined using a least squares method on F^2 , as implemented in Jana2006.⁴²

2.3 Modeling of Disorder in $FASnI_{0.1}Br_{2.9}$:

In the refinement of FASnI_{0.1}Br_{2.9} it was first apparent that a small fraction of iodide was introduced into the structure based on the color of the bulk material with respect to pure FASnBr₃ (Figure 2b/S2). Further evidence in support of iodide substitution came from both the small increase in the unit cell parameters with respect to FASnBr₃ and a measured redshift in the band gap of the material (Figure 9). When introducing I⁻ into the single crystal refinement, it became necessary to disorder the halide site. This was achieved by relaxing the positional constraints initially present which forced the Br⁻ and I⁻ to occupy the same atomic coordinates within the structure. With this applied constraint, the crystallographic refinement was unstable. However, after refining the two positions separately, the two halides were found to occupy different positions, stabilizing the refinement with a small fraction of I⁻. Based on the observed shift in the band gap of the material as well as elemental confirmation of the presence of I⁻ from SEM-EDS, the disorder was kept in the final refinement.

2.4 Modeling of Disorder in $FASnI_{0.4}Br_{2.6}$ (260 K):

During the refinement of the 260 K structure of FASnI_{0.4}Br_{2.6}, it became necessary to disorder the halide positions. The disorder was first realized with a non-negligible residual electron density in the vicinity of the initial halide position. Mixing the halide site (I/Br) and relaxing the constraints on the coordinates showed that I and Br occupied different average positions in the crystal lattice and proved to resolve the residual electron density near the halide site. Despite achieving a reasonable refinement with the above disorder, the model could prove to be inadequate to describe the true average structure of the material. Since the phase transition involves the elongation of 3 bonds in octahedra and a shortening of the remaining 3, induced twinning via different local variations of the transition could yield an average crystal structure with multiple disordered mixed I/Br positions. There can also be a convolution of the antiferroelectric (off-centering) and antiferrodistortive (tilting) distortions, adding additional complexity to the refinement and making a fully detailed refinement difficult. This type of disorder was further confirmed through room temperature pair distribution function (PDF) measurements.

2.5 Steady-state and time-resolved photoluminescence (PL, TRPL):

PL and TRPL spectra of the film samples were measured using an Edinburgh Instruments FS5 Spectrofluorometer. The samples were excited by ps pulsed diode laser. (375 nm excitation

wavelength, pulse width of less than 100 ps and repetition rate 5MHz). The spectra were corrected for the monochromator wavelength dependence and photomultiplier response functions provided by the manufacturer. Measurements were performed using dried polycrystalline powder samples and films. The measured TRPL decay (I(t)) of each sample was fitted by a three-exponent function, convoluted with the measured instrument response function. (t) = × e- $t/\tau i$ + b, τi and ai are the lifetime and amplitude of the different decay components, and b is the background level. The ratio of photons emitted by each component (Phi) can be calculated by $Phi = (ai \times \tau i)/(a1 \times \tau 1 + a2 \times \tau 2 + a3 \times \tau 3)$, (i = 1,2,3), The average lifetime of each sample τavg is defined by $\tau avg = \sum Phi \times \tau i$.

2.6 Perovskite film preparation:

The perovskite stock solutions were prepared by dissolving FAI, FABr, SnI₂ and SnBr₂ precursors with the target composition to form stoichiometric 0.8M FASn(I_{1-x}Br_x)₃ in dimethylformamide (DMF)/dimethyl sulfoxide (DMSO) (3:2 volume ratio) mixed solvent. After the precursor was completely dissolved, the prepared solution was spin-coated on the substrate at 1000 rpm for 10 seconds and 4000 rpm for 30 seconds. Chlorobenzene was added as an antisolvent 25 seconds in the second step. Subsequently, the film was annealed at 100°C for 10 minutes. To mitigate the effect of exposure to ambient conditions, PMMA was spin-coated on thin films to form the final encapsulation layer. All film preparation procedures were conducted in a N₂-filled glove box. The light illumination study was conducted in the glovebox (Figure S11). The thin films were taken out of the glovebox for measurements after each period of illumination under 1sun.

2.7 Pair Distribution Function (PDF) of $FASnI_{3-x}Br_x$ (x = 0, 1.1, 2.6, 3):

Freshly synthesized material was dried under a vacuum and transferred to a nitrogen-filled glovebox. The dried crystallites were then ground in an agate mortar and pestle until a powder-like consistency was achieved. The powder was sieved to 53 μ m particle sizes to ensure dense packing and then transferred to either a quartz or borosilicate capillary with outer diameter dimensions of 0.5 mm (purchased from Charles supper Co.) that was sealed at one end. Once packed, the capillary was sealed and transported to the diffractometer for measurement. Intensity data was collected using a STOE StadiVari diffractometer (detailed in the SXRD section) using 2-hour exposure time per frame, collecting data from 1-160° 2θ (Ag K_{α}) over five frames. Data was

also collected for an empty capillary and air-scattering to establish a background effectively subtracting their scattering contributions. The images were imported into GSAS-II⁴⁴ where instrument parameters were calibrated against a LaB₆ standard collection at the same detector distance. Each frame was integrated as implemented in GSAS-II. The resulting diffraction pattern was exported and manually scaled. The 1D diffraction patterns were reduced to the G(r) in PDFgetX3.⁴⁵ Further details are described in the supporting information.

2.8 Solid-state NMR spectroscopy:

All NMR spectra were acquired on polycrystalline materials. Samples were separately packed into airtight zirconia rotors with an outer diameter of 1.3 mm fitted with VESPEL® caps. Magic-Angle Spinning (MAS) NMR experiments were carried out at 18.8 T on a Bruker Avance Neo NMR spectrometer (the Larmor frequencies were ${}^{1}H = 800.1$ MHz, and ${}^{119}Sn = 298.4$ MHz, respectively) equipped with a 1.3-mm H-X double resonance probe head tuned to ¹H and ¹¹⁹Sn configuration. Unless otherwise specified, all the samples were spun at a MAS frequency of 50 kHz using N_2 gas to prevent the moisture-induced degradation during the data acquisition. The 1D ¹¹⁹Sn MAS NMR spectra were acquired using spin-echo pulse sequence, in which the echo delay was set to 20 microseconds corresponding to one rotor period. For pure FASnI₃ and FASnBr₃ compounds, the ¹¹⁹Sn MAS NMR spectra were acquired by co-adding 2048 transients. For FASnI_{1.1}Br_{1.9} and FASnI_{0.4}Br_{2.6} alloys, the 1D ¹¹⁹Sn MAS NMR spectra were acquired by coadding 2048, using a recycle delay of 3 s ($T_1 \sim 1.4$ s). All 1D ¹H MAS NMR spectra were acquired by 32 co-added transients, whereby the recycle delay was set to 50 s, as determined from saturation recovery measurements and analyses. 2D ¹H-¹H spin diffusion NMR experiments were acquired using three-pulse noesy-like sequence with different mixing times (50, 200 and 500 ms) under fast MAS (55 kHz). A rotor-synchronized increment of 20 us was applied to detect the indirect dimension using $400 t_1$ increments, with 2 co-added transients, leading to an experimental time of ~9 h each. The ¹H experimental shift was calibrated with respect to neat TMS using adamantane as an external reference (¹H resonance, 1.82 ppm). The experimental ¹¹⁹Sn shifts were calibrated using liquid SnCl₂ as an external standard, according to IUPAC recommendation. 46 Data were processed from Bruker Topspin 4.1.4 inbuilt package.

$2.9 \; FASnI_{3-x}Br_x \; (x=0,\,1.1,\,2.6,\,3) \; Raman \; Spectroscopy:$

Selected materials were freshly synthesized using the experimental procedures detailed above and in the supporting information. The synthesized material was then removed from the solution, placed on a piece of filter paper to allow most of the solution to be absorbed and then quickly placed into a 9/7 mm (outer diameter/inner diameter) fused silica tube. The tube was placed under dynamic vacuum for ~24-48 hours, allowing the remainder of the solution to evaporate off. These tubes were then sealed with an O₂/CH₄ torch (vacuum reaching ~10⁻² mbar) and transported to a N₂ filled glovebox. The ampules were opened, and the material was extracted. The compounds were mechanically ground with an agate mortar and pestle and inserted into a quartz cuvette. The powder was more densely packed by adding glass wool, which was added to the cuvette on top of the powder. The top of the cuvette was sealed with epoxy to maintain an inert environment during the measurement. Once the epoxy was cured, the cuvettes were transferred into a plastic bag and vacuum sealed for transportation to the instrument. An example of the sample holders is shown in Figure S12. Raman scattering was collected on these samples using a 660 nm laser on low power settings to avoid laser induced degradation. Raster scans were also utilized for the same purpose. Contributions from the background were then subtracted through a third-order polynomial fit function.

2.10 Computational Methods:

All density functional theory (DFT) calculations were performed using the plane wave code Quantum ESPRESSO.^{47, 48} We employed optimized norm-conserving Vanderbilt pseudopotentials⁴⁹ and the Perdew-Burke-Ernzerhof revised for solids (PBEsol) functional.⁵⁰ We set the kinetic energy cutoff to 120 Ry and fixed the lattice constants of FASnI_{3-x}Br_x for various *x* to the experimental values. To accommodate the Sn lone pairs in FASnI_{3-x}Br_x we employed a 2×2×2 supercell (96 atoms) of the idealized cubic unit cell consisting of 12 atoms [i.e. one formula unit (f.u.)]. This choice of supercell also allowed us to account for local disorder (or polymorphism)⁵¹ in FASnI_{3-x}Br_x, both for the inorganic network and the FA molecules. We stress that employing a random distribution of locally distorted cells in static DFT calculations for halide perovskites has been shown to represent an accurate physical approach to describe the ultraslow structural dynamics, not captured by standard X-ray diffraction.^{51,52} Here, accounting for structural disorder in FASnI₃ leads to a band gap opening at the R point of 0.38 eV (Figure S13b), alleviating the spurious semi-metallic behavior calculated for its high-symmetry counterpart.⁵² We further

achieved randomly disordered structures of all FASnI_{3-x}Br_x compositions via optimization of the nuclear coordinates, following the strategy described by *Zhao* et al.⁵² In our simulations of FASnBr₃, we initially utilized the experimental crystal structure at room temperature, which exhibits the Pa $\overline{3}$ space group. Notably, our DFT optimization of the FASnBr₃ structure to mimic structural disorder preserves the Sn lone pair expression, namely the initial average distortion as obtained from X-ray diffraction. For comparison purposes, we also generated idealized structures of FASnI₃ and FASnBr₃ by fixing the atoms of the inorganic network to their high symmetry Pm $\overline{3}m$ positions and allow the FA⁺ ions to relax. All geometry optimizations were performed using scalar relativistic pseudopotentials.

We employed the band structure unfolding technique to investigate the effect of electronic properties, computed with the inclusion of spin-orbit coupling, of the various compositions in the same Brillouin zone: the fundamental Brillouin zone of an idealized cubic unit cell. Band structure unfolding⁵³ was performed as implemented for plane waves and norm-conserving, fully relativistic pseudopotentials in the ZG module of the EPW code.^{54, 55} Fully-relativistic electron spectral functions of FASnI_{3-x}Br_x compounds were calculated for 300 **k**-points to ensure a correct mapping and dense sampling of the X-R-M-Γ path in the fundamental Brillouin zone of the idealized unit cell. Hole and electron effective masses at the R point were determined by finite differences.

3.0 Results and Discussion

3.1 Synthetic Aspects

Each of the compounds was synthesized from hydrohalic acid mixtures (HI/HBr) by dissolving desired amounts of $SnCl_2 \cdot 2H_2O$ with $FACH_3COO$ followed by cooling the reaction to promote crystallite growth, where the acids were intended to serve as a halide anion source for the perovskite formation. Based on these synthetic conditions necessary to sweep across the $FASnI_3$. $_xBr_x$ (x = 0 - 3) composition space, it became clear that there was a strong preference for the incorporation of I into the structure even with higher relative concentrations of Br in the starting reaction solution.

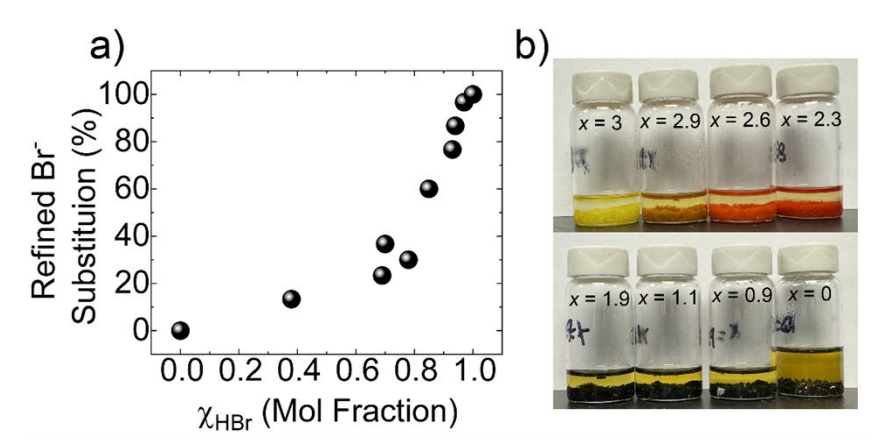


Figure 2: a) A plot of the refined Br stoichiometry based on single crystal X-ray diffraction refinements against the mol fraction (χ_{Br}) of HBr present during the synthesis. Note that the mol fraction only relates the molar ratios of HI and HBr in the reaction solution. b) An image of the bulk material for selected compositions.

This is most evident in the synthesis of FASnI_{1.1}Br_{1.9}, where the refined formula achieved a rough ratio of 2/1 (Br/I). However, during the synthesis, there was an overwhelming excess of Br in the reaction solution (with a mol fraction $\chi_{HBr} = 0.85$). Through experimental findings, it was discovered that only small volumes of hydroiodic acid solution were necessary to isolate materials with high Br concentrations. This fact is supported by the difference in synthetic conditions between FASnI_{0.4}Br_{2.6} and FASnI_{0.1}Br_{2.9}, which were synthesized with only a 0.03 difference in the HBr mol fraction. This relationship is seen when plotting the refined Br stoichiometry against the mol fraction of HBr present during the synthesis (Figure 2a). At low HBr mol fractions $\chi_{\rm HBr}$ (0 – 0.7), there is little change in the refined Br stoichiometry, leading to a maximum of $\sim 1/3$ Br substitution with a 0.7 HBr mol fraction. Within the range of 0.7 – 0.9 HBr, the Br substitution increases an additional 1/3. The final 1/3 substitution is then achieved within a 0.1 HBr mol fraction window, making precise control over the acid volumes paramount to receiving the desired phases. Despite these limited concentration windows, homogenous material with respect to composition was still obtained with single crystal measurements confirming a consistent composition and SEM-EDS providing a composition consistent with refined stoichiometries (Table S5) a within the bounds of the semiquantitative nature of EDS measurements. 2D ¹H-¹H spin diffusion NMR further confirms I/Br intermixing in the bulk sample

suggesting a consistent composition and a lack of phase separation.

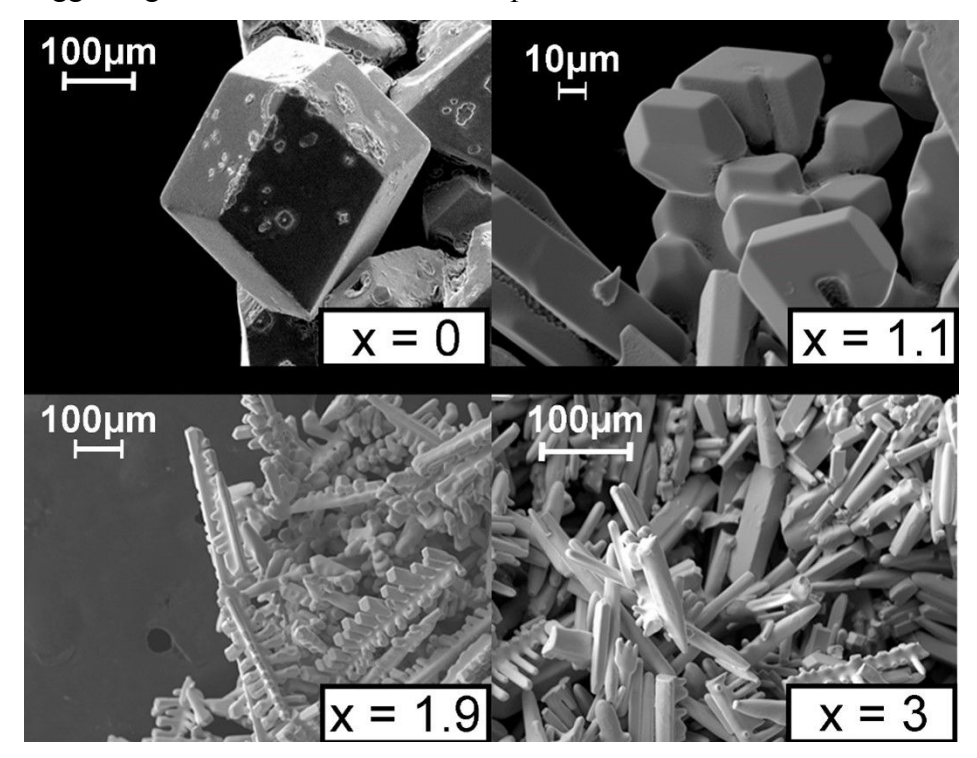


Figure 3: Scanning electron microscopy images of crystallites for selected compositions in the FASnI_{3-x}Br_x (x = 0 - 3) substitution range, showing the typical crystal habit of the materials and their related morphology transition from iodide-rich composition to bromide-rich composition.

During the crystallization process, two additional components play a significant role: the oxidation of Sn^{2+} to Sn^{4+} and the decomposition of formamidine to ammonia. These by-products were observed in excessive amounts during longer crystallization times lasting for 6 hours, with the crystals being cooled down at a rate of 7-10°C/h. We detected the presence of two Sn^{4+} phases: SnI_4 and $(NH_4)_2SnBr_6$. These phases indicate the instability of the Sn^{2+} oxidation state as well as the FA^+ cation, which converted to NH_4^+ ions. For detailed information on the single crystal structure refinement parameters for these secondary phases, please refer to the supporting information (Table S6).

The level of halide mixing also impacted the crystal habit as seen in scanning electron microscopy images of the isolated crystals (Figure 3). FASnI₃ takes on a rhombic dodecahedral shape, typical of 3D hybrid halide perovskite materials. This morphology also agrees with the findings of previous studies of the material.³¹ FASnBr₃, on the other hand, is a rod-like shape that can be generated by elongating the rhombic dodecahedron in a singular direction, creating a crystal shape with a pyramidal-like cap at the end. Noticeably, the crystal habit of the FASnI_{3-x}Br_x phases

shows deviation along these lines with FASnI_{1.9}Br_{1.1} having a morphology more closely resembling FASnI₃ whereas FASnI_{1.1}Br_{1.9} crystallizes with an extended rhombic dodecahedral shape, more closely resembling FASnBr₃. SEM images on the remainder of the compositions confirm the trend in crystal morphology (Figure S3).

3.3.0 Structural Description and Phase Transitions:

The end members of the present series FASnI₃ and FASnBr₃, have previously been structurally characterized through single crystal and Rietveld refinement in previous research efforts.^{31, 32} However, we revisit these two structures as they pertain to their solid solutions.

3.3.1 Structural Description of FASnI₃: When considering only the crystallographic aspects of FASnI₃, the compound is best described by a cubic structure (space group $Pm\overline{3}m$) adopting the ideal perovskite architecture with SnI₆ octahedra corner sharing in all three crystallographic directions, forming a cage with 180° Sn – I – Sn angles. The FA⁺ cation then sits in the center of the cage to balance the overall negative charge of the framework. This organic cation, though, is heavily disordered, intended to represent the dynamic nature of the position of the cation (tumbling). Based on the symmetrical constraints of the space group, the disorder generates a pseudo carbon-centered "octahedra" where the caps are 1/3 occupied N atoms. This type of model is an approximation to the rotation where the molecule which creates a "sphere" of electron density surrounding the central carbon atom. This model, however, does not abide by traditional chemical understanding since the structure of the organic FA⁺ cation is not considered. Alternatively, since FA⁺ has a net dipole moment that cannot be canceled out (as might be suggested by the $Pm\overline{3}m$ model) the symmetry can be reduced to non-centrosymmetric (Amm2), allowing for ordering the FA⁺ cations. This symmetry setting is artificial, however, so the cubic model ($Pm\overline{3}m$) will be considered in further discussions.

It should be noted that FASnI₃ (as well as MASnI₃) undergoes a smooth phase transition at low temperatures characterized in calorimetric measurements by weak endothermic peaks and a long tail at the lower temperature.³² This behavior in Pb-based compounds is commonly associated with antiferrodistortive instabilities on cooling from elevated temperatures, which result in the transition to tetragonal or orthorhombic structures at lower temperatures. From the symmetry viewpoint, these antiferrodistortive and non-polar instabilities are characterized by the M_3^+ and R_4^+ irreducible representations of the $Pm\overline{3}m$ parent phase.⁵⁶ These order parameters are attributed

by symmetry to octahedra rotations at the microscopic level. They are indeed associated experimentally to anisotropic thermal motions with large amplitudes of the halide atoms perpendicular to the metal halide bonds,⁵⁷ and diffuse scattering rods along the M-R lines in reciprocal space.⁵⁸ The slow dynamics related to these strongly anharmonic octahedra rotations is difficult to capture precisely by diffraction techniques. It led to the proposition of the polymorphous picture for the high temperature $Pm\overline{3}m$ cubic phase, leading to some improvement for the refinement of pair distribution functions (PDF).⁵¹

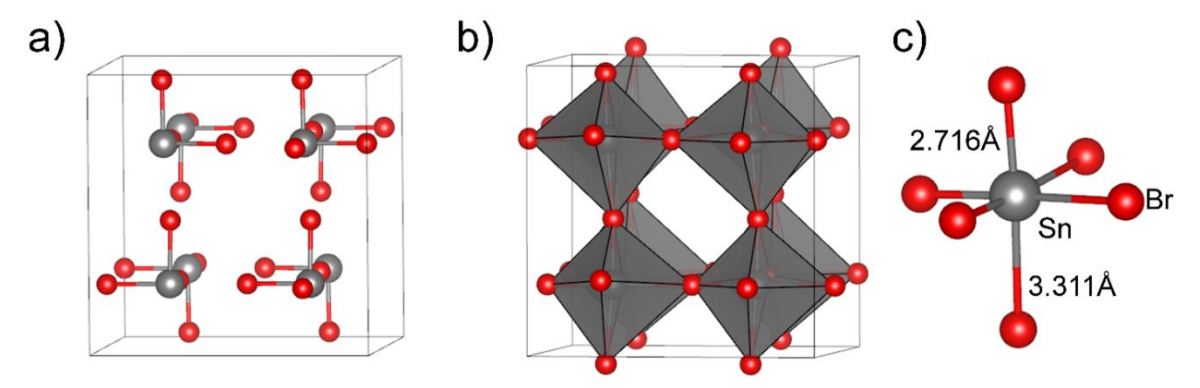


Figure 4: Depiction of the FASnBr₃ structure ($Pa\overline{3}$) in three panels. a) The overall structure with FA⁺ cations omitted for simplicity and b) the same view with polyhedra and elongated bonds included to show how the perovskite framework is retained c) the Sn center with the unique bond distances highlighted. The atoms are presented as grey and red for Sn and Br respectively

 $3.3.2 \, Structural \, Description \, of \, FASnBr_3$: The structure of FASnBr_3 has been resolved from high quality Rietveld refinement previously. However, since our work presents the first single crystal study, we shall endeavor to describe its structure in this section as it is key to understanding structural alterations in FASnI_{3-x}Br_x (x = 0 - 3) phases and drastic deviations in optical properties of these materials. Unlike FASnI₃ the bromide analogue shows increased stereochemical expression of its $5s^2$ loan pair of electrons, which "breaks" the cage framework in an ordered fashion (Figure 4a). 3 of the 6 bonds in the SnBr₆ octahedra extend, creating a set of 3 short 2.716(1) Å bonds and 3 long 3.311(1) Å distances (Figure 4c). This perturbation in the perovskite structure creates what can be thought of as [SnBr₃]- molecular units (pyramidal geometry) that are charged balanced with FA+ cations. However, this view is a simplification used here for clarity as the 3.311(1) Å Sn – Br bonds undoubtedly retain bonding-type interactions. The geometric constraints placed on the framework by the size of FA+ are of equal consideration. Being the largest A-site cage cation typically seen in MHP materials, the Sn–Br framework presents the geometric limit for the FA+ cation before the perovskite cage becomes unstable. This [MX₃]- type unit is

not unprecedented in the perovskite ABX₃ stoichiometry as the compounds RbGeBr₃, 60 CsGeX₃ $(X = Cl, Br, I)_{5}^{61}, MAGeI_{3}^{62}, G_{5}^{63} FAGeI_{3}^{63} FAGeI_{5}^{63} FAGe_{0.5}Sn_{0.5}Br_{3}^{64} MAGeBr_{3}^{64} FA_{0.5}MA_{0.5}GeBr_{3}^{64}$ FAGeBr₃,⁶⁴ N(CH₃)₄GeCl₃,⁶⁵ (CH₃)₂NH₂SnBr₃,⁶⁶ (CH₃)₃NH₂SnBr₃,⁶⁷ NH(CH₃)₃SnBr₃,⁶⁸ NH(CH₃)₃SnCl₃,⁶⁸ C(NH₂)₃SnCl₃⁶⁹ and MASnCl₃⁷⁰ display the same "pyramidal" geometry (Table 3). Therefore, FASnBr₃ is more accurately described as an extended 3D framework (pseudo 0D) at room temperature by considering 0D pyramidal [SnBr₃] units more weakly interacting and arranging in the 3D perovskite architecture (Figure 4b). The lone pair-induced structural distortion, which can also be viewed as a second-order antiferroelectric Jahn-Teller distortion reduces the dimensionality of the 3D network, moving it closer to 0D. Furthermore, this is supported by theoretical studies which probed the limit of the perovskite framework in the FAPb_{1-x}Sn_xBr₃ composition space suggesting the dynamic presence of these distortions.⁵⁹ The pseudodimensional reduction also has a direct impact on the symmetry of the compounds, as it crystallizes in the lower symmetry space group $Pa\overline{3}$ resulting in a 2-fold expansion of the unit cell parameters which can easily be seen in the precession images of reciprocal space (Figure S4). The distortion showed by FASnBr₃ can be alleviated by increasing the temperature whereby the typical 3D perovskite framework is obtained above 312 K,32 which in agreement with an analogous phase transition exhibited by the $CsGeX_3$ (X = Cl, Br, I) compositions.

From the symmetry viewpoint, the structural phase transition from the high-temperature $Pm\overline{3}m$ structure to the room-temperature $Pa\overline{3}$ structure is completely different from the non-polar and antiferrodistortive instabilities attributed to M_3^+ and R_4^+ order parameters seen for the low temperature transitions of FASnI₃. The symmetry analysis of the $Pm\overline{3}m/Pa\overline{3}$ group-subgroup relationship reveals that the structural instability is mainly driven by an X_5^- order parameter. Group symmetry thus predicts a polar instability related to the creation of an antiferroelectric array at room temperature. The antiferroelectric pattern is expected to exhibit phase factors for the atomic motions related to the wavevector \vec{k}_X . Among the three atomic sites (A,B,X) usually defining the regular ABX₃ cubic perovskite lattice at high temperature, the A site (FA^+) is not affected by the X_5^- structural instability. In contrast, both the B site (Sn) and the X site (Br) are expected to undergo atomic axial displacement patterns. This feature is in perfect agreement with the reported experimental structure. The condensation at T = 312 K of the X_5^- structural instability in FASnBr₃ has a calorimetric signature, which is also completely different from the signature of the antiferrodistortive instability in FASnI₃. As expected, the thermal motions obtained from X-ray

diffraction also exhibit new features for FASnBr₃ (*vide infra*). Therefore, a competition between polar and non-polar structural instabilities is expected, something commonly observed in perovskite lattices.⁷¹ Experimentally, a complex superposition of structural signatures of different origins is indeed observed (*vide infra*).

3.3.3 Discrepancy Between CsSnBr₃ and FASnBr₃: Besides being fully inorganic and hybrid, respectively, CsSnBr₃ and FASnBr₃ structurally vary from one another at room temperature. CsSnBr₃ retains a 3D perovskite framework and expected $Pm\overline{3}m$ space group symmetry, while FASnBr₃ distorts reducing the symmetry to $Pa\overline{3}$. This difference can be attributed to the difference in "pressure" exerted by the A-site cation on the inorganic framework. Based on the geometric size, FA⁺ within a Sn – Br perovskite framework represents the limit with respect to the tolerance of the perovskite lattice, i.e., the FA⁺ cation is too large at room temperature (253pm).⁷² This is reconciled with FASnBr₃ generating a perovskite framework at higher temperatures whereby the basic cell and cage can expand to more easily accommodate the larger organic. Cs⁺, on the other hand, typically represents the other end of the tolerance spectrum for halide perovskite templating A-site cations (184 pm).⁷³ Therefore, it can more comfortably template a Sn – Br based perovskite. These structural variations highlight the strict size limitations for perovskite forming compositions.

Table 3: A list of compounds that have [MX₃] 0D molecular units with an AMX₃ perovskite stoichiometry and an

extended 3D architecture. Relevant optical properties of each material are also listed.

Formula	Temperature (K)	Band Gap (eV)	Photoluminescence*	Reference
CsGeI ₃	293	1.6	N/A	61
MAGeI ₃	293	1.9	N	62, 63
FAGeI ₃	293	2.2	N	63
CsGeBr ₃	293	2.42	Y	61 64
RbGeBr ₃	293	N/A	N/A	60
MAGeBr ₃	298	2.91	N	64
$FA_{0.5}MA_{0.5}GeBr_3$	298	3.02	N	64
FAGeBr ₃	298	3.13	N	64
CsGeCl ₃	293	3.69	N/A	61
N(CH ₃) ₄ GeCl ₃	293	N/A	N/A	65

FAGe _{0.5} Sn _{0.5} Br ₃	298	2.75	N	64
$FASnI_{0.4}Br_{2.6} \\$	260	N/A	N/A	This Work
$FASnBr_{2.9}I_{0.1} \\$	300	2.05	N	This Work
FASnBr ₃	290	2.24	N	This Work, ⁷⁴
$(CH_3)_2NH_2SnBr_3$	293	N/A	N/A	66
$(CH_3)_3NH_2SnBr_3$	293	N/A	N/A	67
$NH(CH_3)_3SnBr_3$	296	2.76	N/A	68
$NH(CH_3)_3SnCl_3$	296	3.59	N/A	68
$C(NH_2)_3SnCl_3$	295	N/A	N/A	69
$MASnCl_3$	297	3.46	N/A	70, 75

^{*}Photoluminescence is given a Y if the property was observed, a N if it was not, and a N/A if not reported.

3.3.4 Synthetic Insights Garnered from Structure: The structural differences between the two end-member materials might also give insight into the synthetic conditions necessary for synthesizing the FASnI_{3-x}Br_x (x = 0 - 3). As mentioned in the synthetic portion of the discussion, to achieve a material with 2/3 Br substitution or greater (x = 2 - 3) the mol fraction of hydrobromic acid (χ_{HBr}) must be > 0.9. The pronounced inclination towards I during the synthesis process aligns well with the underlying structure. Given that FASnBr₃ possesses more "discrete" [SnBr₃]-pyramidal units, it essentially functions more like a molecular salt, represented as (FA⁺)([SnBr₃]-), and is associated with a comparatively weaker lattice structure. This makes FASnBr₃ more soluble in the polar acidic media employed during the synthesis. In contrast, FASnI₃ features a 3D network of robustly interconnected corner-sharing SnI₆ octahedra, resulting in diminished solubility in polar solvents when compared to FASnBr₃. Therefore, bromide-rich compositions tend to have higher solubility than their iodide-rich counterparts. Such differential solubilities cause compositions with a higher iodide content to precipitate more easily from the solution. It also supports the idea of halide exchange (iodide for bromide) if exposure to the mother liquor is prolonged since, from a solubility perspective, precipitation of I-rich phases is more favorable.

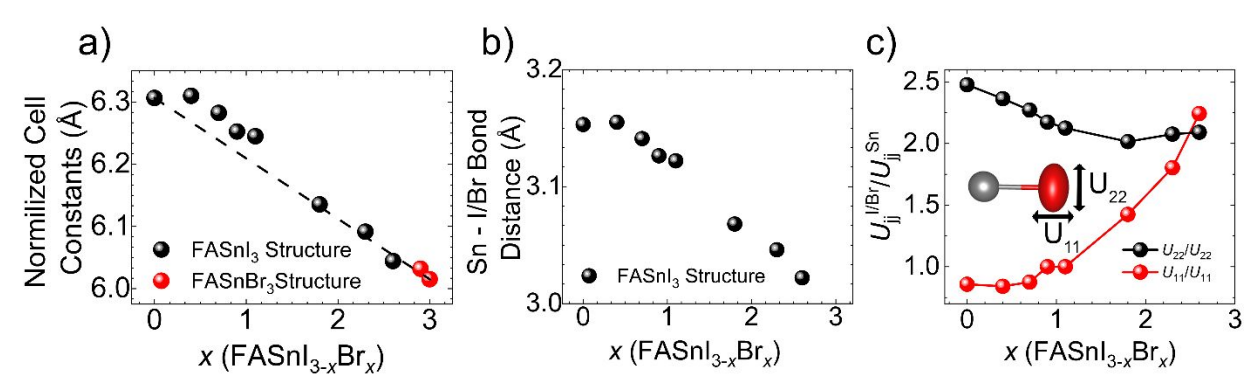


Figure 5: a) The normalized unit cell constants, based on single crystal X-ray diffraction data, for each compound synthesized in the FASnI_{3-x}Br_x (x = 0 - 3) system. Compounds are labeled by their structure type in black and red for the FASnI₃ (Pm $\overline{3}$ m) and FASnBr₃ (Pa $\overline{3}$) structure type, respectively. The dashed line displays the ideal behavior based on Vegard's Law analysis. b) The bond distances for each compound with the FASnI₃ structure plotted against composition. c) A plot of the U_{II} (red) and U_{22} (black) anisotropic displacement parameters as a function of composition normalized to the displacement parameters of the central Sn considering the same direction for all FASnI_{3-x}Br_x compounds that retain the FASnI₃ cubic structure. Note that the U_{22} and the U_{33} parameters are equivalent for both the halide and metal atoms.

3.3.5 Structural Description of the FASnBr₃ (x = 0 - 3) Compositions: Upon the introduction of Br into the structure, there is a corresponding decrease in the unit cell parameters of the cubic structure (denoted as FASnI₃ structure type) following Vegard's Law (Figure 5a). The variations of the standard lattice parameters do not exhibit discontinuities that might attributed to a sudden crossover from a lattice dominated by fluctuations of the octahedra tilts (M_3^+/R_4^+ , FASnI₃.like) to a lattice dominated by atomic translations related to antiferroelectric fluctuations (X_5^- , FASnBr₃.like). The average FASnI₃ structure type was retained for the refinements of the FASnI_{3-x}Br_x (x = 0 - 2.9) structures leading to Br substituted on the I- site and having the same atomic coordinates. Therefore, for these intermediate compositions, the distribution of local static disorder is artificially represented in the refined crystallographic structures through the thermal displacement tensor U_{ij} and is entangled with contributions related to thermal (phonon) displacements.

The inspection of the anisotropic displacement parameters nevertheless allows for the characterization of the interplay between the various (M_3^+/R_4^+) versus X_5^- structural fluctuations. From Figure 5c, we first observe that the U_{22} and U_{33} anisotropic displacement parameters are very strong in FASnI₃ and mainly reflect antiferrodistortive fluctuations related to octahedra rotations. The thermal displacement parameter U_{11} related to axial displacements (stretching of the Sn-I bonds) is smaller by comparison. When the Br content increases, the most noticeable difference is the elongation of the U_{11} thermal displacement parameters from 36(1) to 148(4) Å²x10³ for FASnI₃

and $FASnI_{0.4}Br_{2.6}$ respectively. A very strong increase of the U_{11} parameter is observed for x > 1leading to a maximum value for FASnI_{0.4}Br_{2.6}. The steep increase for intermediate compositions can be partially attributed to the difference in average bond length between Sn – Br and Sn – I and the structural differences between FASnI₃ and FASnBr₃. As the Br increases, the number of [SnBr₃] and [SnIBr₂] units also increase. This leads to a shortening in the bond lengths for regions with this motif and respective lengthening of inter-unit distances. In contrast, the [SnBr₃] and [SnI₂Br] units present in the structure prefer shorter inter-unit distances with small or negligible differences between intra-unit Sn-I and inter-unit Sn-I bonds, thereby forming the connected 3D framework, requiring much longer interatomic distances. This then leads to the apparent elongation of the anisotropic displacement parameter of the halide sites for the Br rich compositions in the cases where the two different halide positions cannot be resolved. This hypothesis is confirmed through low temperature single crystal X-ray diffraction, and room temperature pair distribution function (PDF)/Raman spectroscopy vide infra. The suggestion is also in line with theoretical findings in the FAPb_{1-x}Sn_xBr₃ composition space, which suggest that the off-centering through the lengthening and shortening of bonds is expected to be present up until reaching the Pb-rich regime at which point equalization occurs at FAPb_{0.5}Sn_{0.5}Br_{3.59} The distribution of local static disorder in intermediate compositions is entangled in U_{11} with the contributions related to thermal (phonon) displacements. Both reflect the propensity of the perovskite lattice to undergo locally X_5 structural distortions. It should be noted that the refinements of the average crystallographic structures lead to a clear $Pa\overline{3}$ space group only for very high Br contents. This is expected when the correlation lengths related to the X₅ fluctuations diverge and when the associated diffuse scattering contributions merge into new Bragg-like contributions that can be included in a structure refinement within the $Pa\overline{3}$ space group. It may be further noticed (Figure 5c) that the values of the U₂₂ and U₃₃ anisotropic displacement parameters are only slightly reduced when increasing the Br content by comparison to pure FASnI₃. It suggests that antiferrodistorsive fluctuations are still present whatever the Br content, even when antiferroelectric fluctuations start to dominate.

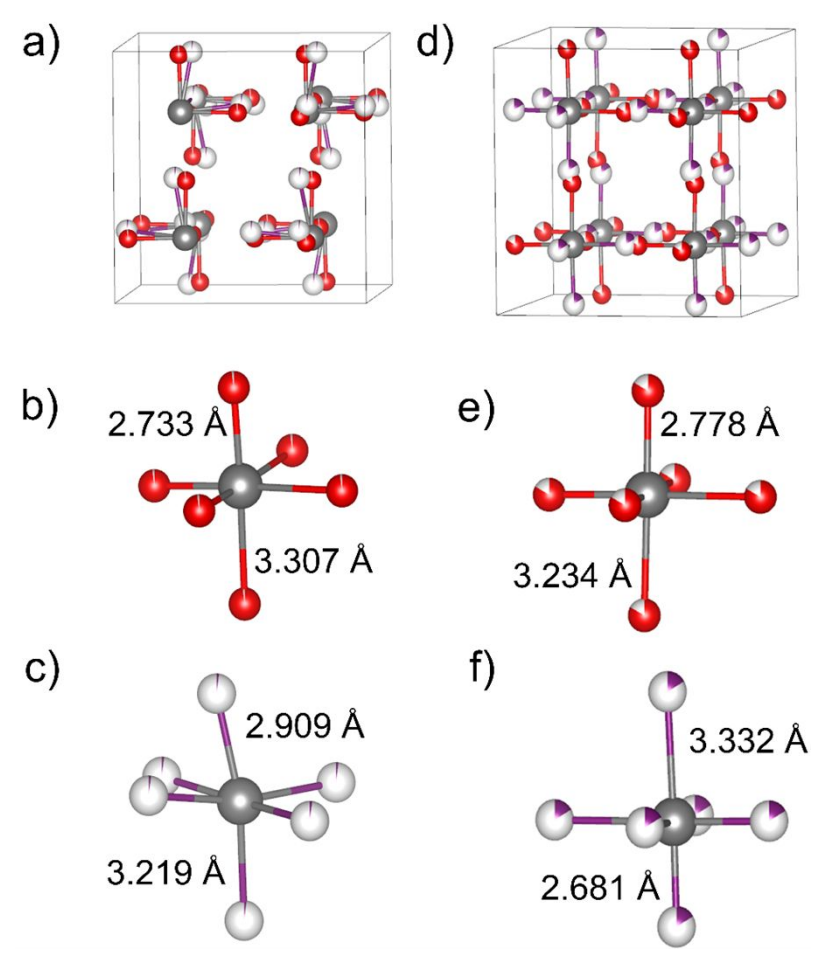


Figure 6: a) depiction of the overall structure of FASnI_{0.1}Br_{2.9} with the organic FA⁺ cations omitted. c) a closer look at the Sn coordination sphere to Br and c) I⁻ for FASnI_{0.1}Br_{2.9}. d) the overall structure of FASnI_{0.4}Br_{2.6} at 260K with the organic cations omitted. e) a closer view of the short and f) long Sn – X distances in FASnI_{0.4}Br_{2.6} at 260K. Both are molded in the $Pa\overline{3}$ space group.

While most of the FASnI_{3-x}Br_x (x = 0 - 3) series retains, on average, the structure of FASnI₃ when x = 2.9 the structure more clearly shifts towards the FASnBr₃ motif but with noticeable differences. FASnI_{0.1}Br_{2.9} crystallizes in the same $Pa\overline{3}$ space group as FASnBr₃ with a 2-fold enlargement of the cell in all three directions; however, the halides are positionally disordered with respect to one another, with the Br and I having independent atomic coordinates (Figure 6a). The disorder allows the small amounts of I⁻ present to modulate its distance from the Sn center. The covalently bonded I atoms obtain a longer bond (2.91(6) Å) compared to an equivalent Br atom (2.733(2) Å) whereas the more non-covalent I atom achieves a shorter distance (3.22(5) Å) than the equivalent Br atom (3.307(3) Å) which is consistent with the I atoms attempting to establish a more stable 3D frameworks compared to the Br atoms, which are stabilized in an extended coordination environment (Figure 6b and 6c).

3.3.6 Temperature-Dependent Phase Transitions: To further investigate the presence of a 3D-0D phase transition, low temperature single crystal X-ray diffraction experiments were conducted on two members of the FASnI_{3-x}Br_x (x = 0 - 3) substitution range, specifically focusing on I-rich and Br-rich compounds that retained the FASnI₃ 3D structure at room temperature. Therefore, FASnI₁₉Br_{1,1} and FASnI_{0,4}Br_{2,6}, were selected as representative candidates. Upon cooling, FASnI_{1.9}Br_{1.1} did not display the anticipated phase change; however, at ~260K the hypothesized 3D-0D transition was observed for FASnI_{0.4}Br_{2.6}, marked by additional reflections in reciprocal space (Figure S10). The resolved structure resembles the room temperature structure FASnI_{0.1}Br_{2.9} with disordered halide positions, but its unique differences (Figure 6d). The best crystallographic model was obtained by relaxing the constraints on the coordinates of I and Br, refining them independently. As a result, the I and Br occupy different positions with two unique interatomic distances to each Sn center each: one bonding (Figure 6e) and one non-bonding distance (Figure 6f). The "bonding" distances are 2.681 Å and 2.778Å for Sn – I and Sn – Br, respectively and the "non-bonding" distances are 3.332 Å and 3.234 Å for Sn – I and Sn – Br, respectively. This places the iodide atoms within bonding distance closer than the bromide and on the opposite side of the octahedra. Note that while these distances are referred to as "bonding" and "non-bonding," the longer distances are expected to have a bonding character, albeit they are much weaker.

While this model achieves reasonable agreement statistics, increased levels of disorder could be present that is not accounted for (see section 2.4). Nonetheless, the presence of the $Pm\overline{3}$ $m/Pa\overline{3}$ structural transition at low temperatures is related to the condensation of the X_5^- structure fluctuations observed at room temperature through the U_{11} parameter (Figure 5c). It confirms that the trend in the room temperature thermal parameters can be attributed to an increased presence of off-centering locally while retaining a 3D framework on average and provides a rationale for observed PL quenching, *vide infra*, as these distortions have already been shown to drastically decrease PL intensity in MAGeI₃.62 Further information on 260K structure of FASnI_{0.4}Br_{2.6} can be found in the supporting information. By conducting additional experiments using temperature-dependent UV-Vis spectroscopy, we can further validate the existence of the phase transition. This confirmation would be evident through the sudden widening of the band gap once the transition temperature is reached on cooling.

3.4. Analyses of the Local Structures for $FASnI_{3-x}Br_x$ (x = 0, 1.1, 2.6, 3) Compositions: Pair Distribution Function (PDF):

To garner a more in-depth understanding of the local structural distortions of the inorganic framework within the mixed halide phases, experimental PDF curves were generated from high-resolution X-ray powder diffraction patterns using equations S1 – S4. Four compositions were selected: FASnI₃ and FASnBr₃, to obtain a baseline PDF curve for the two unique structure types, as well as FASnI_{1.9}Br_{1.1} and FASnI_{0.4}Br_{2.6} since these compositions were tested for temperature-dependent phase transitions through single crystal X-ray diffraction.

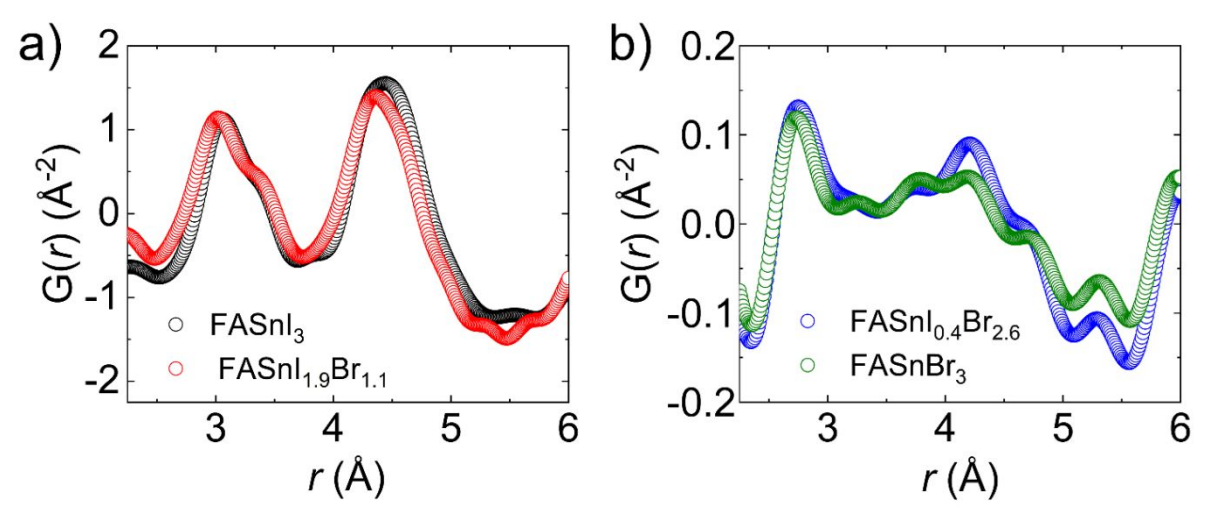


Figure 7: The experimental pair distribution function curves (G(r)) for a) FASnI₃ b) FASnI_{1.9}Br_{1.1} c) FASnI_{0.4}Br_{2.6} and d) FASnBr₃ with the range of 0-6 Å

Experimental PDF curves provide information on the density of atoms present at a distance r (Å) away from an arbitrary center. Based on the average crystal structure for FASnI₃ the local structure of 3D Sn MHP inorganic framework contains two main components consisting of primary distance vectors of ~3 Å and 4.5 Å for Sn – I bonding and I – I nearest neighbors. On the other hand, due to the distortions of the perovskite lattice at room temperature, FASnBr₃ contains two unique Sn – Br distances at 2.7 and 3.3 Å and a broader distribution of nearest neighbor Br – Br vectors providing contrast between the two structure types that can be identified in the G(r). Therefore, examination of the low r regions (2-5 Å) of the PDF curves indicates a distribution of distortions with short coherence lengths. A more extended range of the calculated G(r), however, can be seen in Figure S5

As expected, the experimental PDF of FASnI₃ (Figure 7a) has a strong feature centered at ~ 3 Å. This vector corresponds to the Sn – I bond in the FASnI₃ structure, which deviates ~ 0.1 Å from the distance obtained from the average crystal structure (3.15 Å). However, the position of the peak is consistent with the previous experimental PDF conducted on the same phase. There is, however, identifiable shouldering towards higher r, which could provide evidence for emphanitic behavior: a phenomenon previously identified in the MHP literature despite having roots in chalcogenide chemistry. The experimental PDF also contains a feature centered at 4.5 Å, in line with I – I nearest neighbor distance vectors. Refining the local structure of FASnI₃ by fitting the experimental PDF within the 2-5 Å range shows a reasonable agreement as well as small distortions of the SnI₆ octahedra: off-centering the Sn atom presumably due to activity of the $5s^2$ lone pair (Figure S6). Thus, weak structural fluctuations of the X_5 - type are probably already present in pure FASnI₃ structure.

FASnBr₃, on the other hand, shows a much broader distribution of distance vectors within the 2.5-5 Å region (Figure 7b), suggesting higher degrees of local dynamicity in the Sn – Br bond length as well as other vectors. A sharp feature centering at ~2.7 Å is in excellent agreement with the short, bonding Sn – Br distance. Additionally, broader features at 3.18 and 3.42 Å can be attributed to the long Sn – Br distances in the 0D unit because the average between the two is 3.3 Å. The presence of a split distance vector indicates a higher degree of dynamicity in the 3.311 Å. Broad features in the G(r) between 4 and 5 Å reflect the fluidity in the nearest neighbor Br – Br distance vectors. The fitting of the experimental PDF curve at low r shows that the average crystal structure aligns with the local structure (Figure S7). The curve is also consistent with previous experimental data collected for FASnBr₃, though our local structure explanation differs significantly since here $Pa\overline{3}$ model was used as the basis structure instead of $Pm\overline{3}m$. 81

Comparisons of the mixed halide PDF curves with the end members show a remarkable trend in the short-range structure of these mixed halide phases. The PDF of FASnI_{1.9}Br_{1.1} resembles that of FASnI₃ with a well-resolved peak in the curve at ~3 Å (Figure 7a). Splitting of both the bonding and nearest neighbor halide peaks indicates local discrepancy of these distances, likely associated with mixed I/Br on the halide position. On the other end of the substitution range, FASnI_{0.4}Br_{2.6} displays a curve most similar to that of FASnBr₃ despite the average crystal structure being consistent with FASnI₃. Furthermore, the PDF of this Br-rich phase shows a prominent distance vector at the same 2.7 Å corresponding to the short distance in a [SnBr₃] 0D unit (Figure

7b). The presence of this distance vector indicates a dynamic competition between the concealment and expression of the $5s^2$ lone pair of electrons a local level that is not captured in the average crystal structure, with the exception of the elongation of the displacement parameters. Attempts to model the experimental PDF curves for these mixed halide phases using supercell approximations to the halide substitutions and Reverse Monte Carlo simulations could yield a more in-depth understanding of this competition. Such modeling, however, is outside the scope of the current work. The definitive presence of significant Sn off-centering in the short-range does explain the trends in the optical properties of the bulk materials.

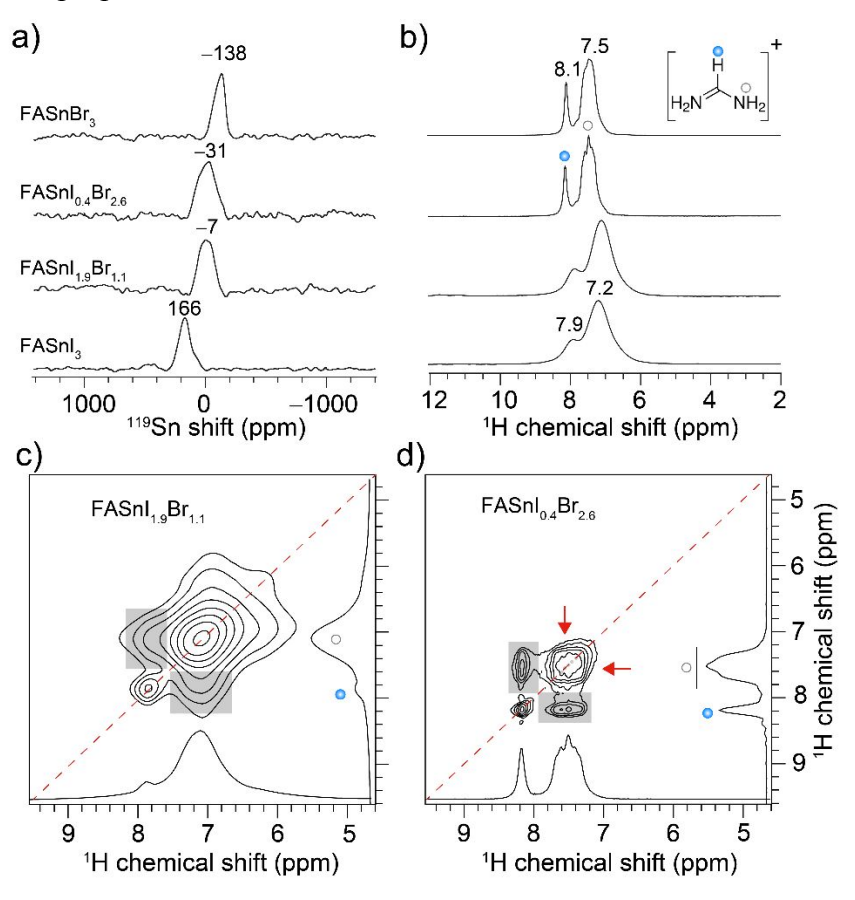


Figure 8: Solid-state 1D (a) 119 Sn and (b) 1 H magic-angle spinning NMR spectra of FASnX₃ alloys as indicated. Solid-state 2D 1 H- 1 H spin-diffusion (SD) NMR spectra of (c) FASnI_{1.9}Br_{1.1} and (d) FASnI_{0.4}Br_{2.6} phases plotted with the sky-line projections presented on horizontal and vertical axes in the insets. All spectra were acquired at 18.8 T (1 H = 800.1 MHz and 119 Sn = 298.4 MHz), 50 kHz (a-b) or 55 kHz (c-d) MAS and at room temperature.

3.4 Solid State ¹¹⁹Sn and ¹H NMR Studies on FASnI_{3-x}Br_x (x = 0, 1.1, 2.6 3):

Solid-state NMR spectroscopy can analyze local chemical environments of organic cations in the cuboctahedral cages and organic-inorganic interfaces, which does not require long-range order.⁸²⁻⁸⁵ Figure 8 presents ¹¹⁹Sn and ¹H spectra of pure phases and alloys. For example, ¹¹⁹Sn

shifts are sensitive to the oxidation state of the Sn atoms, Sn - X bond distances, Sn - X - Sn bond angles and octahedral distortions. The octahedral Sn atoms in the (II) oxidation state produce ¹¹⁹Sn NMR peaks in the range of -1000 and 500 ppm. 86-92 For the 3D FASnI₃ (Figure 8a), the peak centered at 166 ppm is attributed to the Sn atoms in an octahedral coordinated tin iodide network. By comparison, the 3D FASnBr₃ materials produced a peak at -138 ppm due to the Sn atoms coordinated to Br atoms. For the $FASnI_{1.9}Br_{1.1}$ and $FASnI_{0.4}Br_{2.6}$ alloys, the peaks centered at -7 and -31 ppm, respectively, indicate the different local chemical environments of the Sn atoms, which are coordinated to both I and Br sites. The full-width-at-half-maximum (fwhm) values associated with the FASnI_{1.9}Br_{1.1} (fwhm: 178 ppm, ~53 kHz) and FASnI_{0.4}Br_{2.6} (322 ppm, ~96 kHz) compounds, as compared to the pure phases: FASnI₃ (121 ppm, ~36 kHz) and FASnBr₃ (131 ppm, ~36 kHz), further corroborate these results. Specifically, the fwhm of ~322 ppm (96 kHz) in Br-rich phase, which is identical to the chemical shift difference $\Delta\delta(^{119}\text{Sn}) = 304 \text{ ppm } (\sim 91 \text{ kHz})$ between FASnI₃ and FASnBr₃. The different lineshapes associated with the FASnI_{1.9}Br_{1.1} and FASnI_{0.4}Br_{2.6} compounds by means of both chemical shifts and fwhm values suggests halide mixing. It is noteworthy that halide hopping may occur in such species, and degradation products may also form upon exposure to ambient, as previously studied by ssNMR spectroscopy.^{86, 88-90} Additionally, the ¹H NMR spectra of FASnI₃ and FASnI_{1.9}Br_{1.1} phases (Figure 8b) exhibited peaks associated with FA cations corresponding to NH₂ (7.2 ppm) and CH (7.9 ppm) sites. For the FASnI₃ and FASnI_{1.9}Br_{1.1} phases, the relatively narrow features appeared for NH₂ (7.5 ppm) and CH (8.1 ppm) sites. These narrow features indicate the faster re-orientational dynamics of FA⁺ cations in the bromine-rich phases than the iodine-rich phases, due to the different tolerance factors. In addition, the relative difference in the ¹H chemical shifts $\Delta\delta$ ¹H (NH₂) = 0.3 ppm, and $\Delta\delta^{1}H$ (NH) = 0.2 ppm between the bromine-rich and iodine-rich phases indicate the different noncovalent interactions at the organic-inorganic interface. It is noteworthy that the ¹H chemical shifts of the FA⁺ cations FASnI₃ phases (7.2 and 7.9 ppm) are different than the FAPbI₃ phases (7.5 and 8.1), further indicating the different local structures and dynamics of cage cations. 93 The solidstate NMR data reinforces the different local environments for the Sn centers, specifically being well aligned with the distribution of distance vectors in the PDF. The unique ability to probe the organic cation, which is not easily seen through X-ray scattering techniques, adds additional evidence for the above-mentioned structural distortions that increase on a local scale with Br concentration as the FA⁺ cations due to different local chemical environments, with an extended

pseudo-0D framework as opposed to the more rigid SnI₆ cage structure. The different local chemical environments of FA+ and their intermixing nature is further corroborated by analyzing 2D ¹H-¹H spin-diffusion NMR spectra of FASnI_{1.9}Br_{1.1} and FASnI_{0.4}Br_{2.6} compounds. A beneficial feature of 2D ¹H spin diffusion experiment is that it allows spin magnetization to exchange between dipole-dipole coupled ¹H-¹H sites, enabling the through-space proximities between them to probed and distinguished. Close proximities are manifested as off-diagonal peaks, while the ondiagonal peaks are characteristic to chemical shifts. For the I-rich FASnI₁₉Br_{1,1} the SD spectrum acquired with 200 ms showed broad on-diagonal features for NH₂ and CH sites, and the offdiagonal features (gray bands) indicate the strong dipolar interactions between them. By comparison, the Br-rich FASnI_{0.4}Br_{2.6} compound displays narrow features for NH₂ with up to five partially resolved contributions (Figure S8a) due to the different local chemical environments of these sites and CH sites. The well-resolved off-diagonal features between these sites suggests stronger dipolar interactions due to the close inter- and intramolecular proximity. More importantly, the peaks depicted in the red arrows indicate the close proximities between the NH₂ groups in FA cations at different local chemical environments, indicating the intermixing of Br/I halide sites rather than a phase separation. This is further corroborated by acquiring and analyzing the ¹H SD spectra of this latter compound with different spin diffusion mixing times (Figure S8). Overall, the 2D solid-state NMR analysis confirms the different local chemical environments of FA cations and their proximities in I-rich and Br-rich alloys.

3.5. Optical properties:

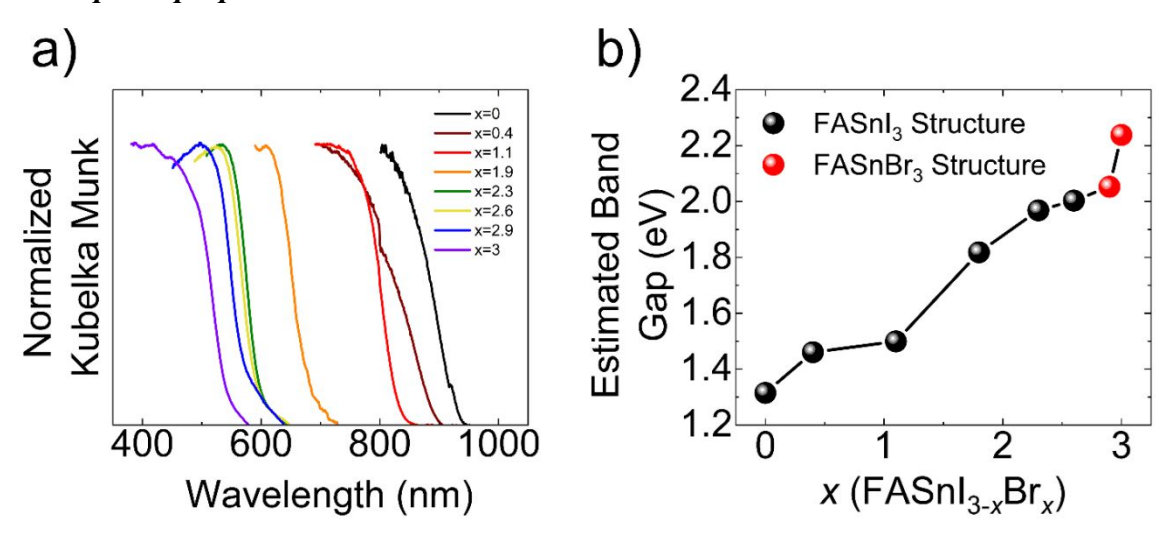


Figure 9: a) Diffuse reflectance UV-Vis spectra for selected compositions, highlighting the positions of the absorption edges and b) the estimated optical band gap for selected compositions in the FASnI_{3-x}Br_x (x = 0 - 3) composition space. The compounds are labeled in black and red depending on if it adopts the FASnI₃ or FASnBr₃ structure type.

3.4.1 Diffuse Reflectance UV-Vis Spectroscopy: The optical diffuse reflectance absorption edges for selected compositions (Figure 9a) shows a blue shifting (widening) of the band gap across the composition space from x = 0 - 3 based on movement of the linear onset of the absorption. The band gap can then be approximated through the linear extrapolation of the linear onset of the absorption with the observed background before the absorption edge. 94 Through this approximation, we estimate the band gap of FASnI₃ to be ~1.31 eV and FASnBr₃ to be ~2.24 eV which is within range of band gaps obtained for these materials in previous works^{31, 32} given that is has been shown that the band gap of hybrid perovskite materials can vary based on the preparation method.³¹ These band gaps values can be compared to both end compositions of their lead counterparts, where FAPbI₃ (α -phase) and FAPbBr₃ have a band gap of 1.48 eV^{31, 34} and 2.30 eV, 95 respectively.

When plotting the estimated gap for the title compounds with respect to composition (Figure 9b), we find that for those compounds that adopt the FASnI₃, $Pm\overline{3}m$, structure there is a near linear behavior consistent with increasing concentrations of the smaller Br frontier orbitals. However, with the shift towards the FASnBr₃, $Pa\overline{3}$, structure, there is a sharp widening of the gap from 2.05 to 2.24 eV, which the disruption in the structure can explain. As 3 of the 6 bonds elongate, the overall orbital overlap of the material drastically decreases, leading to a sharp decrease in the band dispersion. Such an explanation is confirmed through the calculation of the band structures (*vide infra*). Therefore, the FASnBr₃ compositions can be considered the extreme example where the overlap is removed almost entirely for half of the Sn – X bonds. This idea can also be reconciled with other studies on "hollow" perovskites where substitution of [MX₆] octahedra for an organic molecule leads to a blue shifting of the gap as the overall orbital overlap between the metal and halide reduces with increased substitution levels.^{85, 96}

These trends can also be compared with that of CsSnBr₃ with its 3D perovskite structure.⁷⁷ The observed difference in bandgap between both ends of halide members in our compounds is 0.93 eV: 1.31 eV for FASnI₃ compared to 2.24 eV for FASnBr₃. This can be compared to a 0.6 eV difference in the cesium lead halide perovskites: 1.68eV band gap for black CsPbI₃⁹⁷ and 2.29 eV for CsPbBr₃.⁹⁸ Another relatively smaller difference in bandgap is 0.47eV when comparing the bandgaps of CsPbBr₃ (2.29 eV) and CsSnBr₃ (1.82 eV).^{77, 99} We therefore attribute the higher

bandgap difference in our compounds between the bromide and iodide compounds to the emerged structural changes leading to the disconnection of the proper 3D perovskite network.

3.4.2 Photoluminescence Spectroscopy: The Photoluminescence (PL) spectroscopy for selected compositions was performed using thin film samples (Figure 10a). A stock solution of 0.8M was used for spin coating the tin perovskite thin films in the glovebox. Given the enhanced sensitivity of the PL measurement for thin films, our PL measurements on thin films gave stronger PL peaks compared to powder samples.

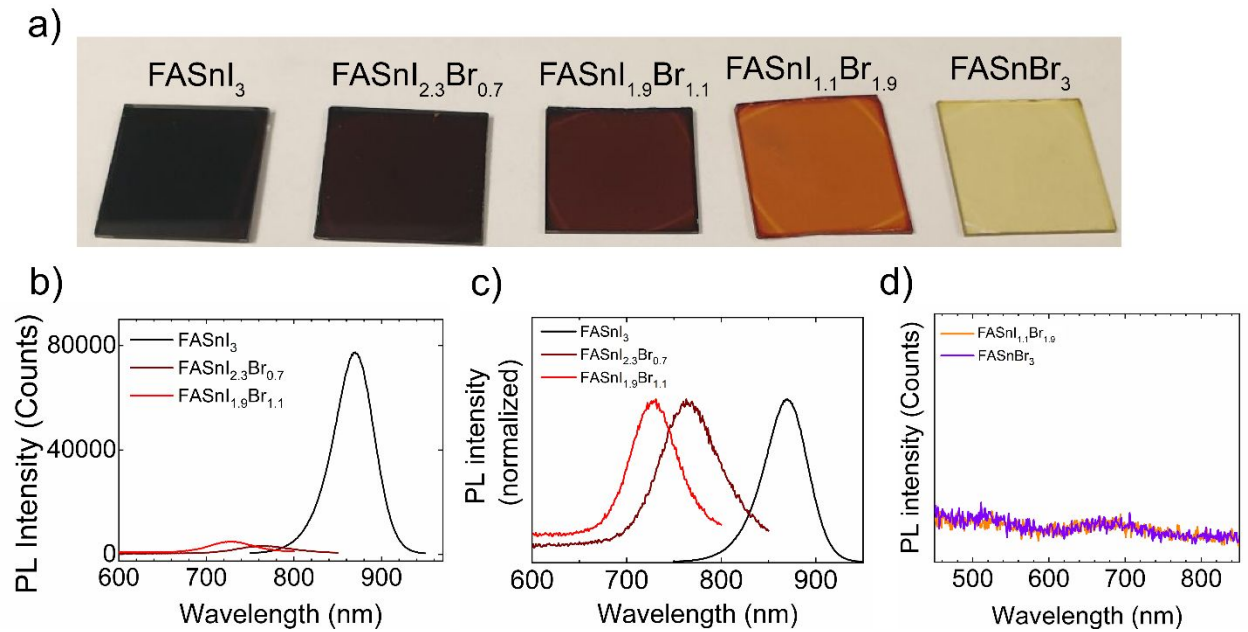


Figure 10: Photoluminescence (PL) of thin films for selected compositions to investigate the PL transition in FASnI_{3-x}Br_x (x = 0 - 3) series, a) an image of representative thin film samples b) PL absolute value spectra showing drastic decrease in intensity with Br incorporation, c) normalized PL spectra of the first three selected composition from iodide rich region, and d) no PL intensity for bromide rich compositions.

For the first three selected samples, the PL peak position increases in energy with respect to composition as the emission was detected at 869 nm, 763 nm, and 729 nm for FASnI₃, FASnI_{2.3}Br_{0.7}, and FASnI_{1.9}Br_{1.1} respectively (Figure 10b, c). These results are in accordance with our optical band gap measurements on these samples. However, as the concentration of incorporated bromide into the crystalline structure increased, there was a drastic quenching of the PL intensity. Comparing the PL intensity of FASnI₃ vs FASnI_{2.3}Br_{0.7} (Figure 10b) more than 90% of the observed intensity was lost. This quenching effect increased as PL emission fell below the background for FASnI_{1.1}Br_{1.9} and FASnBr₃. (Figure 10d). Time-resolved photoluminescence (TRPL) spectra showed a significant drop in PL lifetime by increasing the bromide concentration.

The FASnI_{2.3}Br_{0.7}, and FASnI_{1.9}Br_{1.1} samples have a lifetime shorter than 1 nanosecond and their decay curve interferes with the width of our instrument response function (IRF). (Figure S9).

The strong structural transitions induced by increasing the concentration of bromide can be the origin of the observed PL quenching and reduced lifetime. Through the compositional changes from iodide rich phase to bromide rich phase, the dominance of the pseudo 0D [SnBr₃] molecular units (antiferroelectric distortions) across the lattice was observed rather than cornersharing [SnBr₆]⁴⁻ octahedral units. As discussed in the structural section, these changes happen when 3 of the 6 bonds in the SnBr₆ octahedra extend to make room for the lone pair. Formation of these isolated [SnBr₃] structural units limits the charge transfer across the lattice, increasing the non-radiative recombination and eventually leading to quenching of the PL intensity. In contrast, the perovskite structure of three-dimensional CsSnBr₃ possesses corner-sharing SnBr₆ units and shows photoluminescence.⁷⁷ The observed structural transition in FASnBr₃ and the evolution of isolated more [SnBr₃]- units can be attributed to the presence of FA cation, which is bulkier (with an effective radius of 258 pm)⁷² compared to Cs (184 pm)⁷³ leading to deformation of [SnX₆]⁴- octahedral units by decreasing the size of halide and the cavity between the corner shared units.

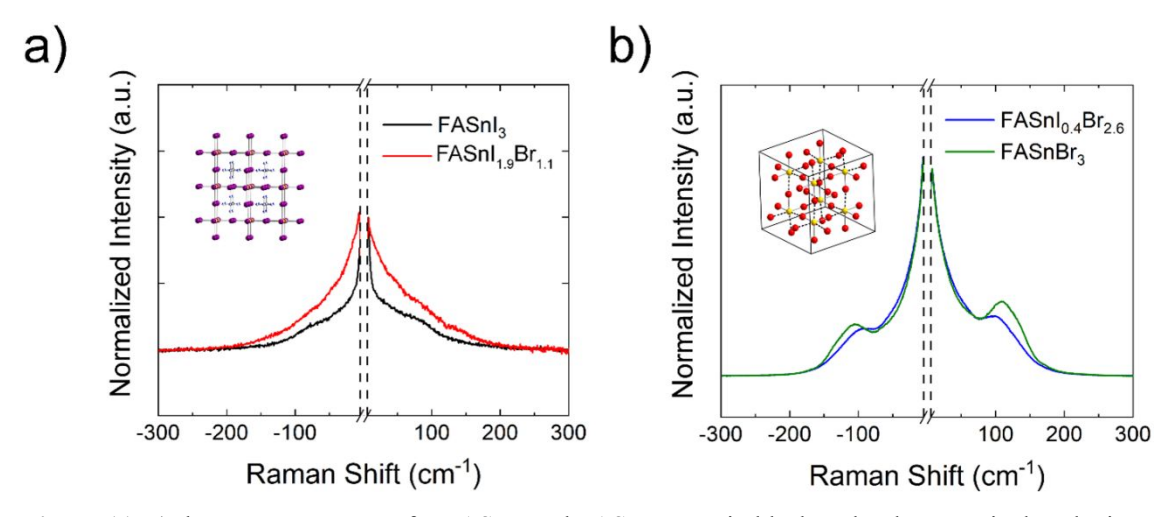


Figure 11: a) the Raman spectrum for FASnI₃ and FASnI_{1.9}Br_{1.1} in black and red, respectively. The inset shows the 3D FASnI₃ perovskite structure. b) the Raman spectrum of FASnI_{0.4}Br_{2.6} and FASnBr₃ in blue and green, respectively. The inset depicts the FASnBr₃ 0D structure. Both graphs have the -7 - 7 cm⁻¹ range omitted to remove the intensity from the excitation laser.

These results are in accordance with pressure-induced structural changes that directly impact the optoelectronic properties of tin bromide compounds.⁷⁴ Moreover, the Ge off-centering observed in germanium iodide perovskites (with different cations, FA, MA or Cs) was observed leading to undetectable PL intensity for this material at ambient conditions while higher pressure-

induced recovery of 3D structure and improving related PL intensity.⁶² While similar pressure-induced phase transitions studies were performed on tin halide perovskites,⁷⁴ to our knowledge, no studies have been done on the mixed halide (specifically FASnI_{3-x}Br_x) compositions. We eagerly propose performing this study where our results indicate similar PL behavior will be observed. To investigate the mechanism of PL quenching further, low frequency Raman spectroscopy was conducted on select samples.

3.4.3 Raman Spectroscopy: Given the presence of structural differences between FASnI₃ and FASnBr₃, the observed temperature-dependent phase transition of FASnI_{0.4}Br_{2.6}, deviation in the local inorganic framework, and the complete PL quenching for samples having Br fractions exceeding and including x = 1.9, room temperature low frequency Raman spectroscopy was conducted on 4 select samples to confirm further a lattice distortions characteristic of the Pa $\overline{3}$ phase for compositions that retain an average 3D perovskite structure at room temperature. Presented in Figure 11, spectra for FASnI₃ and FASnBr₃ were collected to form a baseline for the two different structural variations as well as for FASnI_{1.9}Br_{1.1} and FASnI_{0.4}Br_{2.6} since these compositions were structurally studied at low temperatures through single crystal X-ray diffraction and retain an average 3D structure at room temperature.

The vibrational density of states of hybrid halide perovskites typically exhibit 3 different regions based on the shift, with the regions being well defined for the Pb analogues: $10 - 50 \text{ cm}^{-1}$ (PbX₆ lattice modes mostly related to octahedra rotations), $50\text{-}500 \text{ cm}^{-1}$ (coupled lattice and organic modes, including Pb - X stretching modes), and $500\text{-}3500 \text{ cm}^{-1}$ (individual molecular modes). Here we present data within the two spectral ranges corresponding to the lattice and organic-lattice coupled vibrational modes within the 7-300 cm⁻¹ range. The Raman scattering selection rules for the $Pm\overline{3}m$ perovskite lattice indicates that in the harmonic approximation, no lattice optical modes should be Raman active. These selection rules can be broken when anharmonic and relaxation processes are present, leading to quasi-elastic signatures in hybrid and inorganic perovskites. The observed spectrum of FASnI₃ is consistent with this behavior (Figure 11a), were A small contribution appears around 88 cm⁻¹ as a shoulder. It is attributed to the Raman activation of a lattice mode by anharmonic processes. This broadness at low frequencies highlights the dynamicity of the inorganic lattice and is similar to other hybrid halide perovskite materials that have been studied previously. $^{100, 102, 103}$ FASnBr₃ similarly to FASnI₃ is broad at

very low energies, suggesting the same dynamicity for the inorganic framework, likely caused by relaxation processes related to local rotations. Additionally, there is a sharper, more intense higher energy feature centered around 110 cm⁻¹. Studies conducted on MASnI₃ would suggest that this stretch corresponds to a vibration mode of the organic coupled with Sn – Br stretching..¹⁰⁴ However, studies conducted by Gao, *et al.* on the CsMBr₃ family (M = Ge, Sn, Pb) suggest a more adequate assignment of this feature to structural distortions due to expression of 5*s*-electron lone pairs of Sn. A similar, albeit higher energy, feature is experimentally observed in the Raman scattering of CsGeBr₃ assigned to Ge off-centering.¹⁰⁵ The observation of the 110 cm⁻¹ feature fits nicely with the assignment of the $Pa\overline{3}$ space group, where Raman scattering selection rules are different and optical lattice modes can be observed even in the harmonic approximation. It should also be noted that the components and irreducible representations of the Raman modes can be mapped using a similar methodology used to analyze the CsGeX₃ (X = I, Br, Cl) series, ¹⁰⁶ but such analysis falls outside the scope of the presented work.

The I-rich and Br-rich compounds tested in the FASnI_{3-r}Br_r (x = 0 - 3) mixed halide space showed identical behavior to the end member closest to in composition (Figure 11a & 11b). FASnI_{1.9}Br_{1.1} has a broad spectrum with a slightly more intense peak at the lowest energies. This supports the idea that the structure does not locally distort with appreciable concentrations for the experiment since a high intensity feature around 90-110 cm⁻¹ is not present. FASnI_{0.4}Br_{2.6}, on the other hand, displays nearly identical behavior to FASnBr₃ with a higher energy feature, which is slightly broadened and shifted to lower energies (peak center around 99 cm⁻¹). The shift and broadening of the peak are consistent with both the incorporation of increased I- fractions, as the Sn – I bond is weaker and longer than the Sn – Br bond, and the reduction of distortions. The presence of this feature does, however, support the presence of relatively isolated pyramidal-like structural units which get more numerous with higher bromide concentration (See the related peak in Raman spectra of FASnI_{0.4}Br_{2.6} and FASnBr₃ in Figure 11b). The distribution of local low symmetry lattice distortions is leading to the breaking of the Raman selection rules despite the refinement of the average crystal structure in a $Pm\overline{3}m$ space group. Combining these findings with the conclusions drawn by the room temperature and low temperature single crystal diffraction experiments indicates that although the lattice is dynamic and maintains a 3D structure, the Sn lone pairs locally compete for their own space. Further theoretical studies into the vibrational modes of these mixed halide compositions could verify the assignments of these peaks.

3.6 Photostability of $FASnI_{3-x}Br_x$ Films:

The photostability of mixed halide lead perovskite in operational conditions is an important research topic and has been investigated considerably.^{107, 108} A common practice for the synthesis of wide bandgap perovskites (>1.65 eV) is through the substitution of iodide with bromide (more than 20%).¹⁰⁹ These compositions, however, destabilize under prolonged illumination through phase segregation, *i.e.* under light illumination, Iodide-rich and Iodide-poor regions are formed. This phenomenon is called "halide segregation" and can be investigated by the photoluminescence (PL) study of related thin films upon exposure to light.

Here, we studied this phenomenon for the Sn-mixed halide films including FASnI₃, FASnI_{2.6}Br_{0.4}, FASnI_{2.3}Br_{0.7}, and FASnI_{1.9}Br_{1.1}. Since the primary method for observing this halide segregation is observing shifts in the PL peak position, only a limited scope of compositions was studied. The PL peak shift position is a measure of the quantity of iodide-rich phase formed. A detailed description of the film fabrication and the study is presented in the experimental section. The obtained PL spectra of each thin film as a function of illumination time are presented in Figure 12.

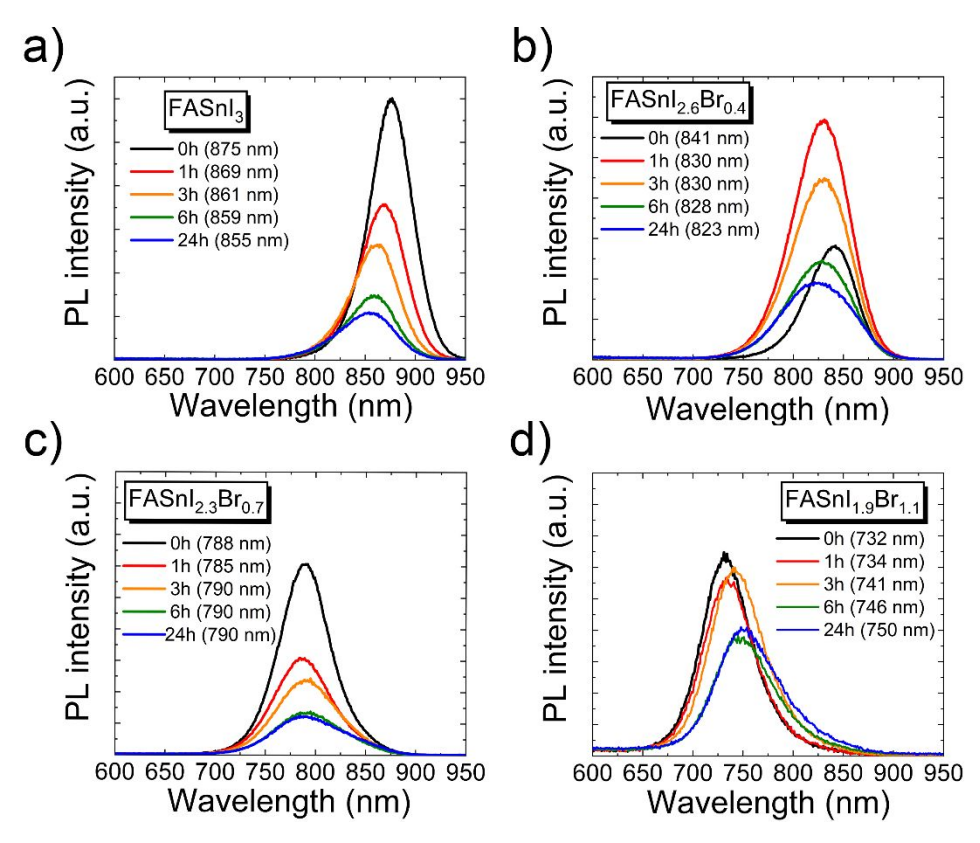


Figure 12 Steady-state PL emission spectra under continuous illumination (a) FASnI_{2.6}Br_{0.4}, (c) FASnI_{2.3}Br_{0.7} and (d) FASnI_{1.9}Br_{1.1}. Each graph presents the PL emission spectra of related films before illumination at 0 time and after 1, 3, 6 and 24 hours of illumination under 1 sun. Detailed PL peak positions are listed in Table S8.

As a general reflection on the PL graphs for all the samples, we observed a decay in PL intensity for all samples after light illumination. This process is typical for perovskite thin films and is often induced by ambient exposure, high temperature, and illumination. For FASnI₃ film a blue shift of 20 nm was observed after 24 hours of illumination, which is solely induced by film degradation under ambient conditions and to a lesser extent induced by high temperature due to light illumination. The ambient exposure in tin perovskites can induce tin (II) partial oxidations to tin (IV) causing such blue shifting.

For the mixed halide phases, peak shifts of 18 nm, 2 nm, and 18 nm were observed for FASnI_{2.6}Br_{0.4}, FASnI_{2.3}Br_{0.7}, and FASnI_{1.9}Br_{1.1} respectively. The observed shift in FASnI_{2.6}Br_{0.4} is towards higher wavelength (similar to that of FASnI₃ thin films) indicating the origin of the shift is degradation of the perovskite films due to ambient atmosphere and heat exposure (rather than halide segregation). Considering the energy difference between the valence band maximum position of iodide rich compositions (compared to that of bromide rich) they are more susceptible to oxidative degradation, hence a blue shift of the PL peak position was observed. A temporary increase in PL intensity is also observed after 1 and 3 hours of illumination. The origins of this, though, would require further investigation but can be referred to light-induce passivation caused by a rapid increase of quasi-fermi level splitting ($\Delta\mu$) which was observed in perovskite mixed halide compositions short after light illumination.^{110, 111} Enhanced PL intensity by increasing the quasi-fermi level splitting is mostly effective in short light illumination time when a limited bandgap shift is detected. Our findings suggest that we observed the same phenomenon where enhanced PL intensity with limited PL peak position was observed after 1 and 3 hours of light soaking.

FASnI_{1.9}Br_{1.1} thin film showed a red shift of 18 nm after 24 hours of illumination. This is indicative of a dominating halide segregation effect due to the formation of iodide-rich regions of the film, which have narrower band gaps and lower energy PL emissions. For FASnI_{2.3}Br_{0.7}, only a 2 nm shift was observed alongside decreased PL intensity, suggesting that both film degradation and halide segregation are occurring simultaneously. This is clear when considering the shape of PL spectra of the FASnI_{2.3}Br_{0.7} composition after illumination, where peak broadening happens for

this specific composition more than others (Figure 12a – d). We detected a FWHM of 62 nm before illumination which gradually increased after light illumination to 86 nm after 24h (Table S9).

These degree of PL peak shifts for these Sn perovskites mimic their lead counterparts, suggesting that these phases may benefit from the same approaches used to control halide segregation investigated for the Pb-based materials such as dimensional control¹¹² or octahedral tilting distortions through structural modifications.^{113, 114}

3.7 Impact of Lone Pair Expression Studied with Density Functional Theory (DFT):

Based on first-principles calculations (see computational details), we investigate the structural and electronic properties of FASnI_{3-x}Br_x, for x = 0, 0.417, 2.583, and 3. We include the effect of local disorder (polymorphism, see computational details) that has been demonstrated to be ubiquitous in perovskite physics to describe the distribution of local octahedra rotations in nominally $Pm\overline{3}m$ structures.⁵² In the case of FASnI₃ and FASnBr₃, accounting for local disorder leads to an energy stabilization of 87.3 meV/f.u. and 124.8 meV/f.u. respectively compared to their idealized Pm $\overline{3}m$ structures. In addition, this computational protocol provides DFT-optimized structures consistent with the experimentally determined averaged structures, exhibiting very clear structural distortions characteristic of stereochemically expressed Sn-5s² lone-pair for FASnBr₃. In contrast, it is found to a lesser extent for FASnI₃ (Figure 12a). Let us note that larger supercells might lead to a better description of the effect in FASnI₃.

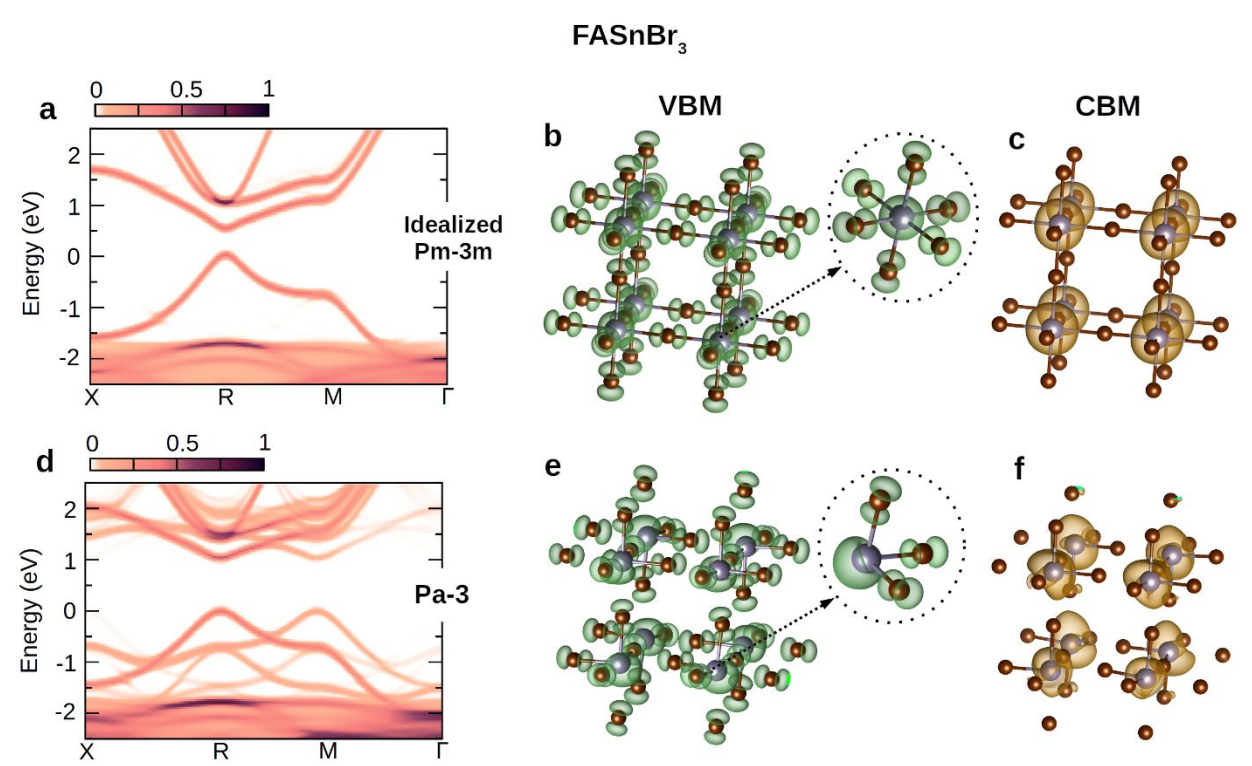


Figure 13: Electronic properties of idealized $(Pm\overline{3}m)$ and distorted $(Pa\overline{3})$ FASnBr₃. Electron spectral functions (color maps) and charge densities of the idealized FASnBr₃ (a,b,c) and distorted FASnBr₃ (d,e,f). Electron spectral functions (a,d) are evaluated using band structure unfolding. The energy axes are adjusted so that the VBM is set at zero energy. Charge densities at the VBM (b,e) and CBM (c,f) are evaluated at the R-point of the fundamental Brillouin zone of the idealized FASnBr₃ $Pm\overline{3}m$ unit cell In the ball and stick models, the FA molecules are removed for clarity.

To ease comparison between the various compositions, we use the band structure unfolding technique, leading to representations of the distorted $Pa\overline{3}$ electronic structure in the Brillouin zone of the parent $Pm\overline{3}m$ structure (Figure 13d). ⁵³ This representation also has the advantage of linking the additional electronic contributions to structural lattice distortions concerning the parent cubic structure. All structures show a direct band gap at the R point. Consistently with experimental findings, increasing the bromine concentration sizably increases the computed fundamental band gap, from 0.38 eV for FASnI₃ to 1.04 eV for FASnBr₃ (Figure S13b-e). Such an increase is expected upon halide substitution. Concomitantly, band curvature at the band edges increases and bands undergo smearing across the Brillouin zone. In order to disentangle the respective effect of local antiferrodistorsive disorder and stereochemical expression of the Sn-5s² lone-pair, we further compare the electronic structure of FASnBr₃ to that of related model structures.

Firstly, the comparison is carried between the momentum-resolved density of states (electron spectral function) computed for FASnBr₃ in the cubic $Pa\overline{3}$ space group with and without taking into account local antiferrodistortive disorder. Both plots show no significant differences

(Figure S14). This suggests this structural disorder does not play a predominant role in the new features observed with increasing bromine content (Figure 13d). Then, to inspect the specific effect of the structural distortion attributed to the lone-pair expression in the $Pa\overline{3}$ structure, we compute the electronic properties of the idealized structure of FASnBr₃ where atoms of the inorganic network are fixed to the Wyckoff positions of the $Pm\overline{3}m$ symmetry (Figure 13a), for which this structural feature is absent. The corresponding electronic structure exhibits a direct band gap of 0.52 eV and hole (electron) effective masses of $m_h = 0.086 \text{ m}_0$ ($m_e = 0.117 \text{ m}_0$), where m_0 is the free electron mass. The charge density plots of the valence band maximum (VBM) and conduction band minimum (CBM) at the R-point reveal that the VBM is determined by the antibonding coupling of the Sn-5s and Br-4p orbitals (Figure 13b), while the CBM mainly stems from Sn-5p orbitals (Figure 13c). Conversely, the corresponding charge densities computed for the $Pa\overline{3}$ structure (Figs. 13e and f, respectively) provide clear evidence of asymmetric charge redistribution due to the lone pair-induced structural distortion. Specifically, the lone pair manifests as an offcenter lobe of electron density around the Sn atom, which diminishes the antibonding interaction between the Sn-5s and Br-4p orbitals in the three shortest Sn – Br bonds. Consequently, the band gap increases markedly to 1.04 eV, alongside a significant change in the effective masses, with the hole mass $m_h = 0.167 m_0$ and $m_e = 0.240 m_0$. The observed energy smearing with the formation of new states at the X and M points (Figure 13d) can also be traced back to the stereochemical expression of the Sn 5s² lone-pair. The formation of these new states at the X and M points can be understood as replicas of the states at the R point induced by lowering the symmetry due to the lone pair-induced lattice distortion. For completeness, we also report the projected density of states calculated for the two structures in Figure S14.

4.0 Conclusions:

The FASnI_{3-x}Br_x (x = 0 - 3) series represents a group of compounds that, on the surface, fulfills the role of a more environmentally sustainable alternative to Pb MHPs given their suitable band gaps for single and multi-junction solar cell devices. However, an in-depth analysis of the structure-property relationships suggests that local structural dynamics leads to the degradation of the coveted optoelectronic properties, namely the photoluminescence and lifetime. The room temperature crystal structures are the first indication of such fluctuations with the phase space behaving as a non-ideal "solid-solution" where the x = 0 - 2.9 compounds crystallize in Pm $\overline{3}m$

while FASnI_{0.1}Br_{2.9} and FASnBr₃ are of lower symmetry (P $a\overline{3}$) due to significant Sn off-centering from $5s^2$ loan pair expression. Probing the local perturbations of the lattice for the I-rich and Brrich regions through Raman scattering and Pair Distribution Function (PDF) elucidates antiferroelectric distortions. The short-range PDF curve for FASnI_{0.4}Br_{0.6} provides the most informative view of the inorganic framework as it is consistent with a FASnBr₃-type structure (P $a\overline{3}$) yet averages to a $Pm\overline{3}m$ structure type. Solid-state ¹¹⁹Sn and ¹H NMR bolster this claim with varying chemical shifts of the Sn and the interrogation of the local structure of the organic. The FA⁺ cation shows sharper features for Br-rich samples as opposed to I-rich mostly likely due to a more loosely connected framework associated with a relatively weaker cage. Competition between the concealment and expression of the Sn lone pair then provides a rationale for the observed PL quenching upon adding Br starting from FASnI₃. Theoretical calculations further support the complex dynamics and the origins of the dissipation of the typically robust PL and electronic properties where the calculated effective mass for both holes and electrons effectively doubles between a hypothetical pristine $Pm\overline{3}m$ and the true distorted $Pa\overline{3}$ structure of FASnBr₃. The phase space may prove to be even more problematic for adoption in photovoltaics given the observation of halide segregation upon light illumination, which was explored for those compounds that showed an observable PL emission above the background. FASnI_{1.9}Br_{1.1} shows a gradual redshifting of the peak position after 0 to 24 hours of 1 sun light exposure, consistent with halide segregation. It remains to be seen, though, if these materials would benefit from the same methods used to mitigate halide segregation of the Pb-based counterparts. This research provides a fundamental guide to synthesizing and characterizing these compounds for further study while simultaneously developing a cautionary stance towards blind assumptions regarding halide perovskite structure and application. To fully grasp the potential applications for these chemically substituted phases, a prior understanding of the fundamental chemical influences at play remains crucial.

Supporting Information:

Additional synthetic procedures and experimental methods, bulk X-ray powder diffraction patterns, additional sample photo for FASnBr₃ and FASnI_{0.1}Br_{2.9}, additional SEM images, reciprocal space images, PDF curves considering an extended range of *r*, fitted PDF curves, 2D ¹H-¹H spin-diffusion (SD) NMR spectrum, time resolved photoluminescence spectra, photo of the

light illumination setup, photo of sample holders used for Raman spectroscopy, additional band structure diagrams and density of states plots, additional crystallographic information tables for the title compounds, the low temperature refinement of FASnI_{0.4}Br_{2.6}, and identified impurity phases, average atomic percentages from SEM-EDS experiments, PL peak position table for light illumination studies, calculated FWHM values for FASnI_{2.3}Br_{0.7} thin films after illumination, and additional references

Acknowledgements:

This work was supported by the US Department of Energy, Office of Science, basic Energy Sciences, under award number DE-SC-0012541 and under the Ultrafast Science Initiative through contract number DE-AC02-06CH11357. Use of the GSECARS Raman Lab System was supported by the NSF MRI Proposal (EAR-1531583). We thank Vitali Prakapenka, Stella Chariton and Young Jay Ryu for assistance with Raman measurements. Work performed at the Center for Nanoscale Materials, a U.S. Department of Energy Office of Science User Facility, was supported by the U.S. DOE, Office of Basic Energy Sciences, under Contract No. DE-AC02-06CH11357. The crystallographic and diffuse reflectance UV-Vis experiments presented in this study made use of the IMSERC Crystallographic and Physical Characterization facilities at Northwestern University, which received support from the Soft and Hybrid Nanotechnology Experimental (SHyNE) resource (NSF ECCS-2025633) and Northwestern University. The silver radiation source used to collect single crystal data on FASnI_{0.1}Br_{2.9} and PDF curves was purchased with the support of the Major Research Instrumentation Program for the National Science Foundation under award CHE-1920248. The SEM-EDS data was gathered at the EPIC facility at Northwestern University's NUANCE Center, which has received support from the SHyNE resource, the IIN, and Northwestern's MRSEC program (NSF DMR-1720139). A.B. was supported by a fellowship through the National Defense Science and Engineering Graduate Fellowship Program (NDSEG), sponsored by the Air Force Research Laboratory (ARFL), the Office of Naval Research (ONR), and the Army Research Office (ARO). M.S. acknowledges financial support from the Swedish research council for sustainable development-Formas (2017-01134) through their "Mobility Starting Grant" program which made it possible to be a visiting scholar at Northwestern University, USA. J.E. acknowledges the Institut universitaire de France. C.W. and G.N.M.R thank the European Union's Horizon 2020 Grant no. 795091 and IR INFRANALYTICS FR2054 for

financial support. M.Z. acknowledges funding from the European Union (project ULTRA-2DPK / HORIZON-MSCA-2022-PF-01 / Grant Agreement No. 101106654). This work was granted access to the HPC resources of TGCC under the allocation 2022-A0110907682 made by GENCI.

Competing Interests:

The authors declare no competing interests.

Data and Materials Availability:

The crystallographic information files (CIFs) for the compounds are available free of charge as depositions in the Cambridge Crystallographic Data Centre (CCDC) based on the following deposition numbers: 2335370 (FASnI₃), 2335364 (FASnI_{2.6}Br_{0.4}), 2335363 (FASnI_{2.3}Br_{0.7}), 2335362 (FASnI_{2.1}Br_{0.9}), 2335361 (FASnI_{1.9}Br_{1.1}), 2335369 (FASnI_{1.1}Br_{1.9}), 2335368 (FASnI_{0.7}Br_{2.3}), 2335367 (FASnI_{0.4}Br_{2.6}; 295K), 2335360 (FASnI_{0.4}Br_{2.6}; 260K), 2335359 (FASnI_{0.1}Br_{2.9}), 2335358 (FASnBr₃), 2335366 (SnI₄), and 2335365 (NH₄)₂SnBr₆.

The calculations (input and output files) employed for this study will be made available via the NOMAD repository [https://nomad-lab.eu/].

References:

- (1) Xing, G.; Mathews, N.; Sun, S.; Lim, S. S.; Lam, Y. M.; Grätzel, M.; Mhaisalkar, S.; Sum, T.
- C. Long-Range Balanced Electron- and Hole-Transport Lengths in Organic-Inorganic CH₃NH₃PbI₃. *Science* **2013**, *342* (6156), 344-347. DOI: doi:10.1126/science.1243167.
- (2) Dong, Q.; Fang, Y.; Shao, Y.; Mulligan, P.; Qiu, J.; Cao, L.; Huang, J. Electron-hole diffusion lengths in solution-grown CH₃NH₃PbI₃ single crystals. *Science* **2015**, *347* (6225), 967-970. DOI: doi:10.1126/science.aaa5760.
- (3) Yin, W.-J.; Shi, T.; Yan, Y. Unique Properties of Halide Perovskites as Possible Origins of the Superior Solar Cell Performance. *Advanced Materials* **2014**, *26* (27), 4653-4658. DOI: https://doi.org/10.1002/adma.201306281.
- (4) Motta, C.; El-Mellouhi, F.; Sanvito, S. Charge carrier mobility in hybrid halide perovskites. *Scientific Reports* **2015**, *5* (1), 12746. DOI: 10.1038/srep12746.
- (5) Roy, P.; Kumar Sinha, N.; Tiwari, S.; Khare, A. A review on perovskite solar cells: Evolution of architecture, fabrication techniques, commercialization issues and status. *Solar Energy* **2020**, *198*, 665-688. DOI: https://doi.org/10.1016/j.solener.2020.01.080.
- (6) Stoumpos, C. C.; Kanatzidis, M. G. Halide Perovskites: Poor Man's High-Performance Semiconductors. *Advanced Materials* **2016**, *28* (28), 5778-5793. DOI: https://doi.org/10.1002/adma.201600265.
- (7) Stoumpos, C. C.; Kanatzidis, M. G. The Renaissance of Halide Perovskites and Their Evolution as Emerging Semiconductors. In *Accounts of Chemical Research*, 2015; Vol. 48, pp 2791-2802.
- (8) Chung, I.; Lee, B.; He, J. Q.; Chang, R. P. H.; Kanatzidis, M. G. All-solid-state dye-sensitized solar cells with high efficiency. *Nature* **2012**, *485* (7399), 486-U494. DOI: 10.1038/nature11067.
- (9) Lee, M. M.; Teuscher, J.; Miyasaka, T.; Murakami, T. N.; Snaith, H. J. Efficient Hybrid Solar Cells Based on Meso-Superstructured Organometal Halide Perovskites. *Science* **2012**, *338* (6107), 643-647. DOI: 10.1126/science.1228604.
- (10) Wang, R.; Mujahid, M.; Duan, Y.; Wang, Z. K.; Xue, J.; Yang, Y. A Review of Perovskites Solar Cell Stability. *Advanced Functional Materials* **2019**, *29* (47), 1808843. DOI: 10.1002/adfm.201808843.
- (11) Peng, W.; Mao, K.; Cai, F.; Meng, H.; Zhu, Z.; Li, T.; Yuan, S.; Xu, Z.; Feng, X.; Xu, J.; et al. Reducing nonradiative recombination in perovskite solar cells with a porous insulator contact. *Science* **2023**, *379* (6633), 683-690. DOI: doi:10.1126/science.ade3126.

- (12) Park, J.; Kim, J.; Yun, H.-S.; Paik, M. J.; Noh, E.; Mun, H. J.; Kim, M. G.; Shin, T. J.; Seok, S. I. Controlled growth of perovskite layers with volatile alkylammonium chlorides. *Nature* **2023**, *616* (7958), 724-730. DOI: 10.1038/s41586-023-05825-y.
- (13) Zhao, Y.; Ma, F.; Qu, Z.; Yu, S.; Shen, T.; Deng, H.-X.; Chu, X.; Peng, X.; Yuan, Y.; Zhang, X.; et al. Inactive (PbI₂)₂RbCl stabilizes perovskite films for efficient solar cells. *Science* **2022**, *377* (6605), 531-534. DOI: doi:10.1126/science.abp8873.
- (14) *Best Researhc-Cell Efficiency Chart*. The National Renewable Energy Labratory, 2024. https://www.nrel.gov/pv/cell-efficiency.html (accessed 2024 02/03/2024).
- (15) Noh, J. H.; Im, S. H.; Heo, J. H.; Mandal, T. N.; Seok, S. I. Chemical Management for Colorful, Efficient, and Stable Inorganic–Organic Hybrid Nanostructured Solar Cells. *Nano Letters* **2013**, *13* (4), 1764-1769. DOI: 10.1021/nl400349b.
- (16) Gil-Escrig, L.; Dreessen, C.; Palazon, F.; Hawash, Z.; Moons, E.; Albrecht, S.; Sessolo, M.; Bolink, H. J. Efficient Wide-Bandgap Mixed-Cation and Mixed-Halide Perovskite Solar Cells by Vacuum Deposition. *ACS Energy Letters* **2021**, *6* (2), 827-836. DOI: 10.1021/acsenergylett.0c02445.
- (17) Hao, F.; Stoumpos, C. C.; Chang, R. P. H.; Kanatzidis, M. G. Anomalous Band Gap Behavior in Mixed Sn and Pb Perovskites Enables Broadening of Absorption Spectrum in Solar Cells. *Journal of the American Chemical Society* **2014**, *136* (22), 8094-8099. DOI: 10.1021/ja5033259.
- (18) Masi, S.; Gualdrón-Reyes, A. F.; Mora-Seró, I. Stabilization of Black Perovskite Phase in FAPbI₃ and CsPbI₃. *ACS Energy Letters* **2020**, *5* (6), 1974-1985. DOI: 10.1021/acsenergylett.0c00801.
- (19) Chin, X. Y.; Turkay, D.; Steele, J. A.; Tabean, S.; Eswara, S.; Mensi, M.; Fiala, P.; Wolff, C. M.; Paracchino, A.; Artuk, K.; et al. Interface passivation for 31.25%-efficient perovskite/silicon tandem solar cells. *Science* **2023**, *381* (6653), 59-63. DOI: doi:10.1126/science.adg0091.
- (20) Hoke, E. T.; Slotcavage, D. J.; Dohner, E. R.; Bowring, A. R.; Karunadasa, H. I.; McGehee, M. D. Reversible photo-induced trap formation in mixed-halide hybrid perovskites for photovoltaics. *Chemical Science* **2015**, *6* (1), 613-617, 10.1039/C4SC03141E. DOI: 10.1039/C4SC03141E.
- (21) Slotcavage, D. J.; Karunadasa, H. I.; McGehee, M. D. Light-Induced Phase Segregation in Halide-Perovskite Absorbers. *ACS Energy Letters* **2016**, *1* (6), 1199-1205. DOI: 10.1021/acsenergylett.6b00495.

- (22) DuBose, J. T.; Kamat, P. V. Hole Trapping in Halide Perovskites Induces Phase Segregation. *Accounts of Materials Research* **2022**, *3* (7), 761-771. DOI: 10.1021/accountsmr.2c00076.
- (23) McMeekin, D. P.; Sadoughi, G.; Rehman, W.; Eperon, G. E.; Saliba, M.; Hörantner, M. T.; Haghighirad, A.; Sakai, N.; Korte, L.; Rech, B.; et al. A mixed-cation lead mixed-halide perovskite absorber for tandem solar cells. *Science* **2016**, *351* (6269), 151-155. DOI: 10.1126/science.aad5845.
- (24) Tan, H. R.; Jain, A.; Voznyy, O.; Lan, X. Z.; de Arquer, F. P. G.; Fan, J. Z.; Quintero-Bermudez, R.; Yuan, M. J.; Zhang, B.; Zhao, Y. C.; et al. Efficient and stable solution-processed planar perovskite solar cells via contact passivation. *Science* **2017**, *355* (6326), 722-726. DOI: 10.1126/science.aai9081.
- (25) Chen, H.; Maxwell, A.; Li, C. W.; Teale, S.; Chen, B.; Zhu, T.; Ugur, E.; Harrison, G.; Grater, L.; Wang, J. K.; et al. Regulating surface potential maximizes voltage in all-perovskite tandems. *Nature* **2023**, *613* (7945), 676-+. DOI: 10.1038/s41586-022-05541-z.
- (26) Abate, A. Perovskite Solar Cells Go Lead Free. *Joule* **2017**, *1* (4), 659-664. DOI: https://doi.org/10.1016/j.joule.2017.09.007.
- (27) Lye, Y.-E.; Chan, K.-Y.; Ng, Z.-N. A Review on the Progress, Challenges, and Performances of Tin-Based Perovskite Solar Cells. *Nanomaterials* **2023**, *13* (3), 585.
- (28) Ke, W.; Stoumpos, C. C.; Kanatzidis, M. G. "Unleaded" Perovskites: Status Quo and Future Prospects of Tin-Based Perovskite Solar Cells. *Advanced Materials* **2019**, *31* (47), 1803230. DOI: https://doi.org/10.1002/adma.201803230.
- (29) Ke, W.; Kanatzidis, M. G. Prospects for low-toxicity lead-free perovskite solar cells. *Nature Communications* **2019**, *10* (1), 965. DOI: 10.1038/s41467-019-08918-3.
- (30) Abate, A. Stable Tin-Based Perovskite Solar Cells. *ACS Energy Letters* **2023**, *8* (4), 1896-1899. DOI: 10.1021/acsenergylett.3c00282.
- (31) Stoumpos, C. C.; Malliakas, C. D.; Kanatzidis, M. G. Semiconducting Tin and Lead Iodide Perovskites with Organic Cations: Phase Transitions, High Mobilities, and Near-Infrared Photoluminescent Properties. In *Inorganic Chemistry*, 2013; Vol. 52, pp 9019-9038.
- (32) Yamada, K.; Fujise, K.; Hino, S.; Yamane, Y.; Nakagama, T. Characterization of Sn(II)-based Perovskites by XRD, DTA, NQR and ¹¹⁹Sn NMR for Photovoltaic Applications. *Chemistry Letters* **2019**, *48* (7). DOI: https://doi.org/10.1246/cl.190262.

- (33) Sadhanala, A.; Deschler, F.; Thomas, T. H.; Dutton, S. E.; Goedel, K. C.; Hanusch, F. C.; Lai, M. L.; Steiner, U.; Bein, T.; Docampo, P.; et al. Preparation of Single-Phase Films of $CH_3NH_3Pb(I_{1-x}Br_{x)3}$ with Sharp Optical Band Edges. *The Journal of Physical Chemistry Letters* **2014**, *5* (15), 2501-2505. DOI: 10.1021/jz501332v.
- (34) Eperon, G. E.; Stranks, S. D.; Menelaou, C.; Johnston, M. B.; Herz, L. M.; Snaith, H. J. Formamidinium lead trihalide: a broadly tunable perovskite for efficient planar heterojunction solar cells. *Energy & Environmental Science* **2014**, *7* (3), 982-988, 10.1039/C3EE43822H. DOI: 10.1039/C3EE43822H.
- (35) Li, X.; Hoffman, J. M.; Kanatzidis, M. G. The 2D Halide Perovskite Rulebook: How the Spacer Influences Everything from the Structure to Optoelectronic Device Efficiency. *Chemical Reviews* **2021**, *121* (4), 2230-2291. DOI: https://doi.org/10.1021/acs.chemrev.0c01006.
- (36) Stoumpos, C. C.; Cao, D. H.; Clark, D. J.; Young, J.; Rondinelli, J. M.; Jang, J. I.; Hupp, J. T.; Kanatzidis, M. G. Ruddlesden–Popper Hybrid Lead Iodide Perovskite 2D Homologous Semiconductors. *Chemistry of Materials* **2016**, *28* (8), 2852-2867. DOI: 10.1021/acs.chemmater.6b00847.
- (37) Vasileiadou, E. S.; Hadar, I.; Kepenekian, M.; Even, J.; Tu, Q.; Malliakas, C. D.; Friedrich, D.; Spanopoulos, I.; Hoffman, J. M.; Dravid, V. P.; et al. Shedding Light on the Stability and Structure–Property Relationships of Two-Dimensional Hybrid Lead Bromide Perovskites. *Chemistry of Materials* **2021**, *33* (13), 5085-5107. DOI: 10.1021/acs.chemmater.1c01129.
- (38) Koziskova, J.; Hahn, F.; Richter, J.; Kožíšek, J. Comparison of different absorption corrections on the model structure of tetrakis(μ 2 -acetato)-diaqua-di-copper(II). In *Acta Chimica Slovaca*, 2016; Vol. 9, pp 136-140.
- (39) Dolomanov, O. V.; Bourhis, L. J.; Gildea, R. J.; Howard, J. A. K.; Puschmann, H. OLEX2: a complete structure solution, refinment and analysis program. *Journal of Applied Crystallography* **2009**, *42* (2), 339-341. DOI: https://doi.org/10.1107/S0021889808042726.
- (40) Sheldrick, G. M. SHELXT Integrated space-group and crystal-structure determination. *Acta Crystallographica A* **2015**, *A71*, 3-8. DOI: https://doi.org/10.1107/S2053273314026370.
- (41) Sheldrick, G. M. Crystal structure refinement with SHELXL. *Acta Crystallographica C* **2014**, *C71* (1), 3-8. DOI: https://doi.org/10.1107/S2053229614024218.

- (42) Petříček, V.; Dušek, M.; Palatinus, L. Crystallographic Computing System JANA2006: General features. *Zeitschrift für Kristallographie Crystalline Materials* **2014**, *229*, 345-352. DOI: 10.1515/zkri-2014-1737.
- (43) Palatinus, L.; Chapuis, G. SUPERFLIP a computer program for the solution of crystal structures by charge flipping in arbitrary dimensions. *Journal of Applied Crystallography* **2007**, *40*, 786-790. DOI: 10.1107/S0021889807029238.
- (44) Andrews, R. H.; Clark, S. J.; Donaldson, J. D.; Dewan, J. C.; Silver, J. Solid-state properties of materials of the type Cs_4MX_6 (where M = Sn or Pb and X = Cl or Br). *Journal of the Chemical Society, Dalton Transactions* **1983**, (4), 767. DOI: 10.1039/dt9830000767.
- (45) Juhas, P.; Davis, T.; Farrow, C. L.; Billinge, S. J. L. PDFgetX3: a rapid and highly automatable program for processing powder diffraction data into total scattering pair distribution functions. *Journal of Applied Crystallography* **2013**, *46* (2), 560-566. DOI: doi:10.1107/S0021889813005190.
- (46) Harris, R. K.; Becker, E. D.; Cabral de Menezes, S. M.; Goodfellow, R.; Granger, P. NMR nomenclature. Nuclear spin properties and conventions for chemical shifts(IUPAC Recommendations 2001). **2001**, *73* (11), 1795-1818. DOI: doi:10.1351/pac200173111795 (accessed 2024-04-16).
- (47) Giannozzi, P.; Baroni, S.; Bonini, N.; Calandra, M.; Car, R.; Cavazzoni, C.; Ceresoli, D.; Chiarotti, G. L.; Cococcioni, M.; Dabo, I.; et al. QUANTUM ESPRESSO: a modular and open-source software project for quantum simulations of materials. *Journal of Physics: Condensed Matter* **2009**, *21* (39), 395502. DOI: 10.1088/0953-8984/21/39/395502.
- (48) Giannozzi, P.; Andreussi, O.; Brumme, T.; Bunau, O.; Buongiorno Nardelli, M.; Calandra, M.; Car, R.; Cavazzoni, C.; Ceresoli, D.; Cococcioni, M.; et al. Advanced capabilities for materials modelling with Quantum ESPRESSO. *Journal of Physics: Condensed Matter* **2017**, *29* (46), 465901. DOI: 10.1088/1361-648X/aa8f79.
- (49) Hamann, D. R. Optimized norm-conserving Vanderbilt pseudopotentials. *Physical Review B* **2013**, *88* (8), 085117. DOI: 10.1103/PhysRevB.88.085117.
- (50) Perdew, J. P.; Ruzsinszky, A.; Csonka, G. I.; Vydrov, O. A.; Scuseria, G. E.; Constantin, L. A.; Zhou, X.; Burke, K. Restoring the Density-Gradient Expansion for Exchange in Solids and Surfaces. *Physical Review Letters* **2008**, *100* (13), 136406. DOI: 10.1103/PhysRevLett.100.136406.

- (51) Zhao, X.-G.; Dalpian, G. M.; Wang, Z.; Zunger, A. Polymorphous nature of cubic halide perovskites. *Physical Review B* **2020**, *101* (15), 155137. DOI: 10.1103/PhysRevB.101.155137.
- (52) Zacharias, M.; Volonakis, G.; Giustino, F.; Even, J. Anharmonic electron-phonon coupling in ultrasoft and locally disordered perovskites. *npj Computational Materials* **2023**, *9* (1), 153. DOI: 10.1038/s41524-023-01089-2.
- (53) Popescu, V.; Zunger, A. Extracting E versus k effective band structure from supercell calculations on alloys and impurities. *Physical Review B* **2012**, *85* (8), 085201. DOI: 10.1103/PhysRevB.85.085201.
- (54) Zacharias, M.; Giustino, F. Theory of the special displacement method for electronic structure calculations at finite temperature. *Physical Review Research* **2020**, *2* (1), 013357. DOI: 10.1103/PhysRevResearch.2.013357.
- (55) Lee, H.; Poncé, S.; Bushick, K.; Hajinazar, S.; Lafuente-Bartolome, J.; Leveillee, J.; Lian, C.; Lihm, J.-M.; Macheda, F.; Mori, H.; et al. Electron–phonon physics from first principles using the EPW code. *npj Computational Materials* **2023**, *9* (1), 156. DOI: 10.1038/s41524-023-01107-3.
- (56) Howard, C. J.; Stokes, H. T. Group-Theoretical Analysis of Octahedral Tilting in Perovskites. *Acta Crystallographica Section B* **1998**, *54* (6), 782-789. DOI: doi:10.1107/S0108768198004200.
- (57) Baikie, T.; Barrow, N. S.; Fang, Y.; Keenan, P. J.; Slater, P. R.; Piltz, R. O.; Gutmann, M.; Mhaisalkar, S. G.; White, T. J. A combined single crystal neutron/X-ray diffraction and solid-state nuclear magnetic resonance study of the hybrid perovskites CH₃NH₃PbX₃ (X = I, Br and Cl). *Journal of Materials Chemistry A* **2015**, *3* (17), 9298-9307, 10.1039/C5TA01125F. DOI: 10.1039/C5TA01125F.
- (58) Lanigan-Atkins, T.; He, X.; Krogstad, M. J.; Pajerowski, D. M.; Abernathy, D. L.; Xu, G. N. M. N.; Xu, Z.; Chung, D. Y.; Kanatzidis, M. G.; Rosenkranz, S.; et al. Two-dimensional overdamped fluctuations of the soft perovskite lattice in CsPbBr₃. *Nature Materials* **2021**, *20* (7), 977-983. DOI: 10.1038/s41563-021-00947-y.
- (59) Pisanu, A.; Mahata, A.; Mosconi, E.; Patrini, M.; Quadrelli, P.; Milanese, C.; De Angelis, F.; Malavasi, L. Exploring the Limits of Three-Dimensional Perovskites: The Case of FAPb_{1-x}Sn_xBr₃. *ACS Energy Letters* **2018**, *3* (6), 1353-1359. DOI: 10.1021/acsenergylett.8b00615.
- (60) Thiele, G.; Rotter, H. W.; Schmidt, K. D. Die Kristallstrukturen und Phasentransformationen von RbGeBr₃. *Zeitschrift für anorganische und allgemeine Chemie* **1988**, *559* (1), 7-16. DOI: https://doi.org/10.1002/zaac.19885590101.

- (61) Thiele, G.; Rotter, H. W.; Schmidt, K. D. Kristallstrukturen und Phasentransformationen von Caesiumtrihalogenogermanaten(II) CsGeX₃ (X = Cl, Br, I). *Zeitschrift fr anorganische und allgemeine Chemie* **1987**, *545* (2), 148-156. DOI: 10.1002/zaac.19875450217.
- (62) Lü, X.; Stoumpos, C.; Hu, Q.; Ma, X.; Zhang, D.; Guo, S.; Hoffman, J.; Bu, K.; Guo, X.; Wang, Y.; et al. Regulating off-centering distortion maximizes photoluminescence in halide perovskites. *National Science Review* **2020**, *8* (9). DOI: 10.1093/nsr/nwaa288 (accessed 6/20/2023).
- (63) Stoumpos, C. C.; Frazer, L.; Clark, D. J.; Kim, Y. S.; Rhim, S. H.; Freeman, A. J.; Ketterson, J. B.; Jang, J. I.; Kanatzidis, M. G. Hybrid Germanium Iodide Perovskite Semiconductors: Active Lone Pairs, Structural Distortions, Direct and Indirect Energy Gaps, and Strong Nonlinear Optical Properties. *Journal of the American Chemical Society* **2015**, *137* (21), 6804-6819. DOI: 10.1021/jacs.5b01025.
- (64) Liu, Y.; Gong, Y. P.; Geng, S.; Feng, M. L.; Manidaki, D.; Deng, Z.; Stoumpos, C. C.; Canepa, P.; Xiao, Z.; Zhang, W. X.; et al. Hybrid Germanium Bromide Perovskites with Tunable Second Harmonic Generation. *Angewandte Chemie International Edition* **2022**, *61* (43). DOI: 10.1002/anie.202208875.
- (65) Depmeier, W.; Moller, A.; Klaska, K.-H. The structure of antiferroelectric tetramethylammonium trichlorogermanate(II) at room temperature. *Acta Crystallographica Section B* **1980**, *36* (4), 803-807. DOI: doi:10.1107/S0567740880004578.
- (66) Thiele, G.; Serr, B. R. Crystal structure of dimethylammonium tribromostannate(II), (CH₃)₂NH₂SnBr₃. *Zeitschrift für Kristallographie Crystalline Materials* **1996**, *211* (1), 47-47. DOI: doi:10.1524/zkri.1996.211.1.47 (accessed 2023-05-11).
- (67) Thiele, G.; Serr, B. R. Crystal structure of trimethylammonium tribromostannate(II), (CH₃)₃NHSnBr₃. **1996**, *211* (1), 46-46. DOI: doi:10.1524/zkri.1996.211.1.46 (accessed 2023-05-11).
- (68) Dang, Y.; Zhong, C.; Zhang, G.; Ju, D.; Wang, L.; Xia, S.; Xia, H.; Tao, X. Crystallographic Investigations into Properties of Acentric Hybrid Perovskite Single Crystals NH(CH₃)₃SnX₃ (X = Cl, Br). *Chemistry of Materials* **2016**, *28* (19), 6968-6974. DOI: 10.1021/acs.chemmater.6b02653. (69) Szafrański, M.; Ståhl, K. Crystal structure and phase transitions in perovskite-like C(NH₂)₃SnCl₃. *Journal of Solid State Chemistry* **2007**, *180* (8), 2209-2215. DOI: https://doi.org/10.1016/j.jssc.2007.05.024.

- (70) Yamada, K.; Kuranaga, Y.; Ueda, K.; Goto, S.; Okuda, T.; Furukawa, Y. Phase Transition and Electric Conductivity of ASnCl3 (A = Cs and CH3NH3). *Bulletin of the Chemical Society of Japan* **1998**, *71* (1), 127-134. DOI: 10.1246/bcsj.71.127 (accessed 4/9/2024).
- (71) Varignon, J.; Bristowe, N. C.; Bousquet, E.; Ghosez, P. Coupling and electrical control of structural, orbital and magnetic orders in perovskites. *Scientific Reports* **2015**, *5* (1), 15364. DOI: 10.1038/srep15364.
- (72) Saparov, B.; Mitzi, D. B. Organic–Inorganic Perovskites: Structural Versatility for Functional Materials Design. *Chemical Reviews* **2016**, *116* (7), 4558-4596. DOI: 10.1021/acs.chemrev.5b00715.
- (73) Kieslich, G.; Sun, S.; Cheetham, A. K. Solid-state principles applied to organic–inorganic perovskites: new tricks for an old dog. *Chemical Science* **2014**, *5* (12), 4712-4715, 10.1039/C4SC02211D. DOI: 10.1039/C4SC02211D.
- (74) Coduri, M.; Shiell, T. B.; Strobel, T. A.; Mahata, A.; Cova, F.; Mosconi, E.; De Angelis, F.; Malavasi, L. Origin of pressure-induced band gap tuning in tin halide perovskites. *Materials Advances* **2020**, *1* (8), 2840-2845, 10.1039/D0MA00731E. DOI: 10.1039/D0MA00731E.
- (75) Yagyu, H.; Katagami, S. Effect of Cs partial substitution on crystal systems and bandgap values of MASnCl3. *Physica B: Condensed Matter* **2022**, *633*, 413784. DOI: https://doi.org/10.1016/j.physb.2022.413784.
- (76) Laurita, G.; Fabini, D. H.; Stoumpos, C. C.; Kanatzidis, M. G.; Seshadri, R. Chemical tuning of dynamic cation off-centering in the cubic phases of hybrid tin and lead halide perovskites. *Chemical Science* **2017**, *8* (8), 5628-5635, 10.1039/C7SC01429E. DOI: 10.1039/C7SC01429E.
- (77) Fabini, D. H.; Laurita, G.; Bechtel, J. S.; Stoumpos, C. C.; Evans, H. A.; Kontos, A. G.; Raptis, Y. S.; Falaras, P.; Van der Ven, A.; Kanatzidis, M. G.; et al. Dynamic Stereochemical Activity of the Sn²⁺ Lone Pair in Perovskite CsSnBr₃. *Journal of the American Chemical Society* **2016**, *138* (36), 11820-11832. DOI: 10.1021/jacs.6b06287.
- (78) Knox, K. R.; Bozin, E. S.; Malliakas, C. D.; Kanatzidis, M. G.; Billinge, S. J. L. Local off-centering symmetry breaking in the high-temperature regime of SnTe. *Physical Review B* **2014**, 89 (1), 014102. DOI: 10.1103/PhysRevB.89.014102.
- (79) Yu, R.; Bozin, E. S.; Abeykoon, M.; Sangiorgio, B.; Spaldin, N. A.; Malliakas, C. D.; Kanatzidis, M. G.; Billinge, S. J. L. Emphanitic anharmonicity in PbSe at high temperature and

- anomalous electronic properties in the PbQ (Q= S, Se, Te) system. *Physical Review B* **2018**, *98* (14), 144108. DOI: 10.1103/PhysRevB.98.144108.
- (80) Xie, H.; Bozin, E. S.; Li, Z.; Abeykoon, M.; Banerjee, S.; Male, J. P.; Snyder, G. J.; Wolverton, C.; Billinge, S. J. L.; Kanatzidis, M. G. Hidden Local Symmetry Breaking in Silver Diamondoid Compounds is Root Cause of Ultralow Thermal Conductivity. *Advanced Materials* **2022**, *34* (24), 2202255. DOI: https://doi.org/10.1002/adma.202202255.
- (81) Morana, M.; Wiktor, J.; Coduri, M.; Chiara, R.; Giacobbe, C.; Bright, E. L.; Ambrosio, F.; De Angelis, F.; Malavasi, L. Cubic or Not Cubic? Combined Experimental and Computational Investigation of the Short-Range Order of Tin Halide Perovskites. *The Journal of Physical Chemistry Letters* **2023**, *14* (8), 2178-2186. DOI: 10.1021/acs.jpclett.3c00105.
- (82) Kubicki, D. J.; Stranks, S. D.; Grey, C. P.; Emsley, L. NMR spectroscopy probes microstructure, dynamics and doping of metal halide perovskites. *Nature Reviews Chemistry* **2021**, *5* (9), 624-645. DOI: 10.1038/s41570-021-00309-x.
- (83) Dahlman, C. J.; Kubicki, D. J.; Reddy, G. N. M. Interfaces in metal halide perovskites probed by solid-state NMR spectroscopy. *Journal of Materials Chemistry A* **2021**, *9* (35), 19206-19244, 10.1039/D1TA03572J. DOI: 10.1039/D1TA03572J.
- (84) Raval, P.; Akhavan Kazemi, M. A.; Ruellou, J.; Trébosc, J.; Lafon, O.; Delevoye, L.; Sauvage, F.; Manjunatha Reddy, G. N. Examining a Year-Long Chemical Degradation Process and Reaction Kinetics in Pristine and Defect-Passivated Lead Halide Perovskites. *Chemistry of Materials* **2023**, *35* (7), 2904-2917. DOI: 10.1021/acs.chemmater.2c03803.
- (85) Spanopoulos, I.; Hadar, I.; Ke, W.; Guo, P.; Mozur, E. M.; Morgan, E.; Wang, S.; Zheng, D.; Padgaonkar, S.; Manjunatha Reddy, G. N.; et al. Tunable Broad Light Emission from 3D "Hollow" Bromide Perovskites through Defect Engineering. *Journal of the American Chemical Society* **2021**, *143* (18), 7069-7080. DOI: 10.1021/jacs.1c01727.
- (86) Kubicki, D. J.; Prochowicz, D.; Salager, E.; Rakhmatullin, A.; Grey, C. P.; Emsley, L.; Stranks, S. D. Local Structure and Dynamics in Methylammonium, Formamidinium, and Cesium Tin(II) Mixed-Halide Perovskites from ¹¹⁹Sn Solid-State NMR. *Journal of the American Chemical Society* **2020**, *142* (17), 7813-7826. DOI: 10.1021/jacs.0c00647.
- (87) Fu, P.; Quintero, M. A.; Vasileiadou, E. S.; Raval, P.; Welton, C.; Kepenekian, M.; Volonakis, G.; Even, J.; Liu, Y.; Malliakas, C.; et al. Chemical Behavior and Local Structure of the

- Ruddlesden–Popper and Dion–Jacobson Alloyed Pb/Sn Bromide 2D Perovskites. *Journal of the American Chemical Society* **2023**, *145* (29), 15997-16014. DOI: 10.1021/jacs.3c03997.
- (88) Karmakar, A.; Mukhopadhyay, S.; Gachod, P. G. B.; Mora-Gomez, V. A.; Bernard, G. M.; Brown, A.; Michaelis, V. K. Uncovering Halogen Mixing and Octahedral Dynamics in Cs₂SnX₆ by Multinuclear Magnetic Resonance Spectroscopy. *Chemistry of Materials* **2021**, *33* (15), 6078-6090. DOI: 10.1021/acs.chemmater.1c01561.
- (89) Karmakar, A.; Bhattacharya, A.; Sarkar, D.; Bernard, G. M.; Mar, A.; Michaelis, V. K. Influence of hidden halogen mobility on local structure of CsSn(Cl_{1-x}Br_x)₃ mixed-halide perovskites by solid-state NMR. *Chemical Science* **2021**, *12* (9), 3253-3263, 10.1039/D0SC05614F. DOI: 10.1039/D0SC05614F.
- (90) Ha, M.; Karmakar, A.; Bernard, G. M.; Basilio, E.; Krishnamurthy, A.; Askar, A. M.; Shankar, K.; Kroeker, S.; Michaelis, V. K. Phase Evolution in Methylammonium Tin Halide Perovskites with Variable Temperature Solid-State 119Sn NMR Spectroscopy. *The Journal of Physical Chemistry C* **2020**, *124* (28), 15015-15027. DOI: 10.1021/acs.jpcc.0c03589.
- (91) Eichler, B. E.; Power, P. P. Characterization of the Sterically Encumbered Terphenyl-Substituted Species 2,6-Trip₂H₃C₆Sn-Sn(Me)₂C₆H₃-2,6-Trip₂, an Unsymmetric, Group 14 Element, Methylmethylene, Valence Isomer of an Alkene, Its Related Lithium Derivative 2,6-Trip₂H₃C₆(Me)₂Sn-Sn(Li)(Me)C₆H₃-2,6-Trip₂, and the Monomer Sn(t-Bu)C₆H₃-2,6-Trip₂ (Trip = C_6 H₂-2,4,6-i-Pr₃). *Inorganic Chemistry* **2000**, *39* (24), 5444-5449. DOI: 10.1021/ic0005137.
- (92) Stückrath, J. B.; Gasevic, T.; Bursch, M.; Grimme, S. Benchmark Study on the Calculation of ¹¹⁹Sn NMR Chemical Shifts. *Inorganic Chemistry* **2022**, *61* (9), 3903-3917. DOI: 10.1021/acs.inorgchem.1c03453.
- (93) Raval, P.; Kennard, R. M.; Vasileiadou, E. S.; Dahlman, C. J.; Spanopoulos, I.; Chabinyc, M. L.; Kanatzidis, M.; Manjunatha Reddy, G. N. Understanding Instability in Formamidinium Lead Halide Perovskites: Kinetics of Transformative Reactions at Grain and Subgrain Boundaries. *ACS Energy Letters* **2022**, *7* (4), 1534-1543. DOI: 10.1021/acsenergylett.2c00140.
- (94) Kortüm, G.; Braun, W.; Herzog, G. Principles and Techniques of Diffuse-Reflectance Spectroscopy. *Angewandte Chemie International Edition in English* **1963**, *2*, 333-341. DOI: 10.1002/anie.196303331.
- (95) Liu, Y.; Cai, B.; Yang, H.; Boschloo, G.; Johansson, E. M. J. Solvent Engineering of Perovskite Crystallization for High Band Gap FAPbBr₃ Perovskite Solar Cells Prepared in

- Ambient Condition. ACS Applied Energy Materials **2023**, 6 (13), 7102-7108. DOI: 10.1021/acsaem.3c00791.
- (96) Spanopoulos, I.; Ke, W.; Stoumpos, C. C.; Schueller, E. C.; Kontsevoi, O. Y.; Seshadri, R.; Kanatzidis, M. G. Unraveling the Chemical Nature of the 3D "Hollow" Hybrid Halide Perovskites. *Journal of the American Chemical Society* **2018**, *140* (17), 5728-5742. DOI: 10.1021/jacs.8b01034.
- (97) Yu, Z.; Leilaeioun, M.; Holman, Z. Selecting tandem partners for silicon solar cells. *Nature Energy* **2016**, *I* (11), 16137. DOI: 10.1038/nenergy.2016.137.
- (98) Straus, D. B.; Cava, R. J. Tuning the Band Gap in the Halide Perovskite CsPbBr₃ through Sr Substitution. *ACS Applied Materials & Interfaces* **2022**, *14* (30), 34884-34890. DOI: 10.1021/acsami.2c09275.
- (99) Heo, J.-M.; Cho, H.; Lee, S.-C.; Park, M.-H.; Kim, J. S.; Kim, H.; Park, J.; Kim, Y.-H.; Yun, H. J.; Yoon, E.; et al. Bright Lead-Free Inorganic CsSnBr₃ Perovskite Light-Emitting Diodes. *ACS Energy Letters* **2022**, *7* (8), 2807-2815. DOI: 10.1021/acsenergylett.2c01010.
- (100) Ibaceta-Jaña, J.; Muydinov, R.; Rosado, P.; Mirhosseini, H.; Chugh, M.; Nazarenko, O.; Dirin, D. N.; Heinrich, D.; Wagner, M. R.; Kühne, T. D.; et al. Vibrational dynamics in lead halide hybrid perovskites investigated by Raman spectroscopy. *Physical Chemistry Chemical Physics* **2020**, *22* (10), 5604-5614, 10.1039/C9CP06568G. DOI: 10.1039/C9CP06568G.
- (101) Létoublon, A.; Paofai, S.; Rufflé, B.; Bourges, P.; Hehlen, B.; Michel, T.; Ecolivet, C.; Durand, O.; Cordier, S.; Katan, C.; et al. Elastic Constants, Optical Phonons, and Molecular Relaxations in the High Temperature Plastic Phase of the CH3NH3PbBr3 Hybrid Perovskite. *The* Journal of Physical Chemistry Letters **2016**, 7 (19), 3776-3784. DOI: 10.1021/acs.jpclett.6b01709. (102) Yaffe, O.; Guo, Y.; Tan, L. Z.; Egger, D. A.; Hull, T.; Stoumpos, C. C.; Zheng, F.; Heinz, T. F.; Kronik, L.; Kanatzidis, M. G.; et al. Local Polar Fluctuations in Lead Halide Perovskite Crystals. **Physical** Review Letters 2017, (13),136001. DOI: 10.1103/PhysRevLett.118.136001.
- (103) Damle, V. H.; Gouda, L.; Tirosh, S.; Tischler, Y. R. Structural Characterization and Room Temperature Low-Frequency Raman Scattering from MAPbI3 Halide Perovskite Films Rigidized by Cesium Incorporation. *ACS Applied Energy Materials* **2018**, *1* (12), 6707-6713. DOI: 10.1021/acsaem.8b01539.

- (104) Badrooj, M.; Jamali-Sheini, F.; Torabi, N. Optoelectronic Properties of Mixed Sn/Pb Perovskite Solar Cells: The Study of Compressive Strain by Raman Modes. *The Journal of Physical Chemistry C* **2020**, *124* (49), 27136-27147. DOI: 10.1021/acs.jpcc.0c07999.
- (105) Gao, L.; Yadgarov, L.; Sharma, R.; Korobko, R.; McCall, K. M.; Fabini, D. H.; Stoumpos, C. C.; Kanatzidis, M. G.; Rappe, A. M.; Yaffe, O. Metal cation s lone-pairs increase octahedral tilting instabilities in halide perovskites. *Materials Advances* **2021**, *2* (14), 4610-4616, 10.1039/D1MA00288K. DOI: 10.1039/D1MA00288K.
- (106) Huang, L.-y.; Lambrecht, W. R. L. Vibrational spectra and nonlinear optical coefficients of rhombohedral $CsGeX_3$ halide compounds with X = I, Br, Cl. *Physical Review B* **2016**, *94* (11), 115202. DOI: 10.1103/PhysRevB.94.115202.
- (107) Motti, S. G.; Patel, J. B.; Oliver, R. D. J.; Snaith, H. J.; Johnston, M. B.; Herz, L. M. Phase segregation in mixed-halide perovskites affects charge-carrier dynamics while preserving mobility. *Nature Communications* **2021**, *12* (1), 6955. DOI: 10.1038/s41467-021-26930-4.
- (108) Lin, Y.; Chen, B.; Fang, Y.; Zhao, J.; Bao, C.; Yu, Z.; Deng, Y.; Rudd, P. N.; Yan, Y.; Yuan, Y.; et al. Excess charge-carrier induced instability of hybrid perovskites. *Nature Communications* **2018**, *9* (1), 4981. DOI: 10.1038/s41467-018-07438-w.
- (109) Kim, D.; Jung, H. J.; Park, I. J.; Larson, B. W.; Dunfield, S. P.; Xiao, C.; Kim, J.; Tong, J.; Boonmongkolras, P.; Ji, S. G.; et al. Efficient, stable silicon tandem cells enabled by anion-engineered wide-bandgap perovskites. *Science* **2020**, *368* (6487), 155-160. DOI: 10.1126/science.aba3433 (acccessed 2024/01/22).
- (110) Cacovich, S.; Messou, D.; Bercegol, A.; Béchu, S.; Yaiche, A.; Shafique, H.; Rousset, J.; Schulz, P.; Bouttemy, M.; Lombez, L. Light-Induced Passivation in Triple Cation Mixed Halide Perovskites: Interplay between Transport Properties and Surface Chemistry. *ACS Applied Materials & Interfaces* **2020**, *12* (31), 34784-34794. DOI: 10.1021/acsami.0c06844.
- (111) Motti, S. G.; Gandini, M.; Barker, A. J.; Ball, J. M.; Srimath Kandada, A. R.; Petrozza, A. Photoinduced Emissive Trap States in Lead Halide Perovskite Semiconductors. *ACS Energy Letters* **2016**, *I* (4), 726-730. DOI: 10.1021/acsenergylett.6b00355.
- (112) Wang, Z.; Lin, Q.; Chmiel, F. P.; Sakai, N.; Herz, L. M.; Snaith, H. J. Efficient ambient-air-stable solar cells with 2D–3D heterostructured butylammonium-caesium-formamidinium lead halide perovskites. *Nature Energy* **2017**, *2* (9), 17135. DOI: 10.1038/nenergy.2017.135.

- (113) Wang, Z.; Zeng, L.; Zhu, T.; Chen, H.; Chen, B.; Kubicki, D. J.; Balvanz, A.; Li, C.; Maxwell, A.; Ugur, E.; et al. Suppressed phase segregation for triple-junction perovskite solar cells. *Nature* **2023**, *618* (7963), 74-79. DOI: 10.1038/s41586-023-06006-7.
- (114) Prasanna, R.; Gold-Parker, A.; Leijtens, T.; Conings, B.; Babayigit, A.; Boyen, H.-G.; Toney, M. F.; McGehee, M. D. Band Gap Tuning via Lattice Contraction and Octahedral Tilting in Perovskite Materials for Photovoltaics. *Journal of the American Chemical Society* **2017**, *139* (32), 11117-11124. DOI: 10.1021/jacs.7b04981.

TOC Graphic:

